

國立交通大學

機械工程學系

博士論文

脈衝式電源驅動之平板型常壓氮氣為主介電質  
電漿的流體模型模擬

**Fluid Modeling of Parallel-plate Nitrogen-based  
Dielectric Barrier Discharge Driven by a  
Realistic Distorted Sinusoidal AC Power Source**

研究生：鄭凱文

指導教授：吳宗信 博士

西元 2012 年 7 月

脈衝式電源驅動之平板型常壓氮氣為主介電質  
電漿的流體模型模擬

**Fluid Modeling of Parallel-plate Nitrogen-based  
Dielectric Barrier Discharge Driven by a  
Realistic Distorted Sinusoidal AC Power Source**

研究生：鄭凱文

Student : Kai-Wen Cheng

指導教授：吳宗信 博士

Advisor : Dr. Jong-Shinn Wu

國立交通大學

機械工程學系

博士論文

A Thesis

Submitted to Department of Mechanical Engineering

College of Engineering

National Chiao Tung University

in Partial Fulfillment of the Requirements

for the Degree of

Doctor of Philosophy

In

Mechanical Engineering

July 2012

Hsinchu, Taiwan

西元 2012 年 7 月

# 脈衝式電源驅動之平板型常壓氮氣為主介電質電漿的流體模型模擬

學生： 鄭凱文

指導教授： 吳宗信 博士

交通大學 機械工程學系

## 摘要

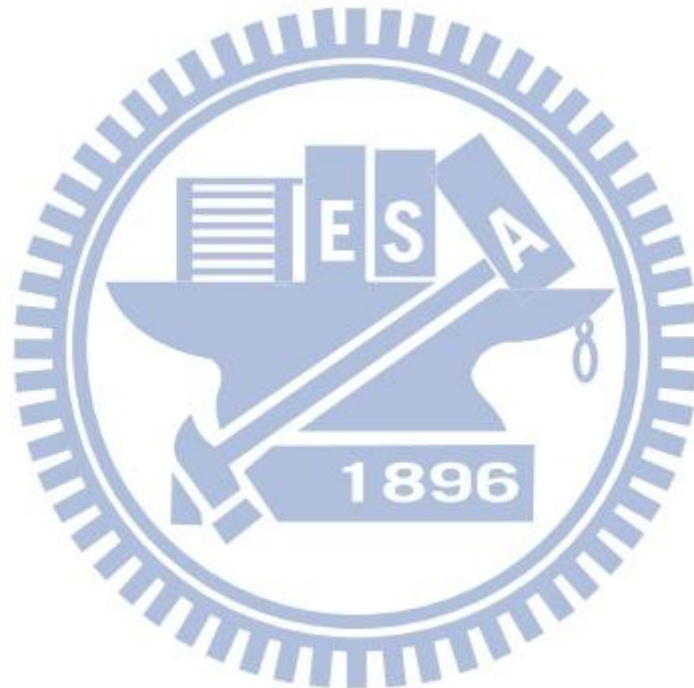
本論文考慮在交流 60 kHz 頻率的條件下，使用流體模型模擬脈衝式電源之平板型氮氣為主的介電質電漿。從數值模擬計算出的電流-電壓曲線，發現在計量上與實驗量測相當符合。

在純氮氣的數值模擬中，可看到  $N_4^+$  離子為電漿濃度最高的帶電粒子。另外改變介電質之間的距離超過 1.0 mm 時，氮氣電漿會從 Townsend-like discharge 轉變成 filamentary-like discharge 型式。實驗量測上也發現同樣的轉變現象。當增加輸入的電壓時，電漿密度與電漿內部吸收的能量也隨之增加。由結果可看到  $N_4^+$  離子獲得最多的能量並且超過電子吸收的十倍以上。介電質材質分析中，介電值壁面上的累積電荷正比於介電常數。由於累積電荷越多，可提供越多離子化時需要的電子，因此較容易維持電漿。另外增加介電質的厚度時對電漿密度與內部能量吸收也有相當大的影響。

當微量的氧氣加入氮氣電漿時，可看到  $N_4^+$  與  $O_2^-$  離子有相同的密度且為電漿濃度最高的帶電粒子。另外發現中性粒子  $N_2(A^3\Sigma_u^+)$  與氮原子的模擬結果與實驗量測非常相近。由於電子會大量吸附在氧氣上，降低電漿內部的電子密度，而使電漿離子化的機率降低。因此可發現隨著氧氣濃度從 0.003 % 增加到 0.1 % 時，電子的密度從  $10^{17} \text{ m}^{-3}$  減少到  $10^{14} \text{ m}^{-3}$ ，並且發現只要加入少量的氧氣就會明顯影響電漿的維持。在光譜的模擬結果上，選擇 second positive system (SPS)、

NO $\gamma$ -system 與 ON $_2$ -excimer 三組光譜與實驗量測作比較。兩者比較結果皆隨著氧氣含量的增加，光譜強度從快速的增加轉變成逐漸的降低。

在論文最後，總結截止目前為止的成果，並提出未來的研究方向與工作。



# **Fluid Modeling of Parallel-plate Nitrogen-based Dielectric Barrier Discharge Driven by a Realistic Distorted Sinusoidal AC Power Source**

Student: Cheng, Kai-Wen

Advisor: Dr. Wu, Jong-Shinn

Department of Mechanical Engineering

National Chiao-Tung University

## **Abstract**

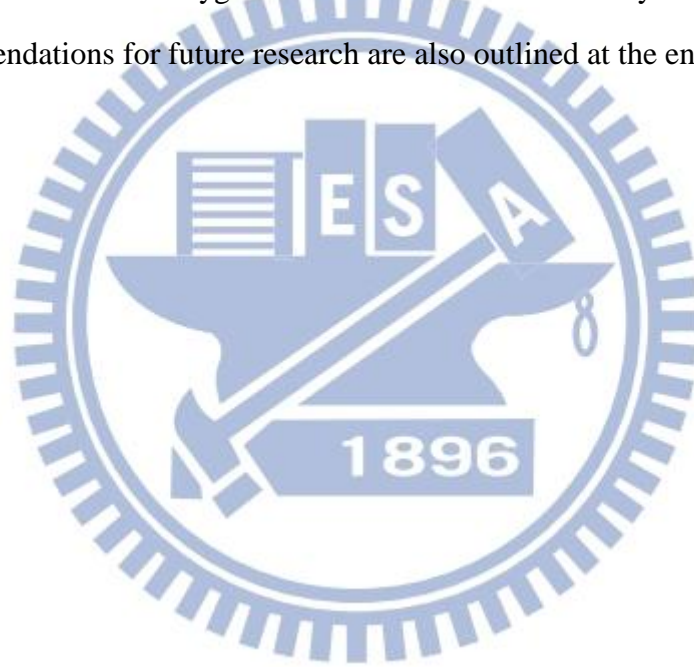
A simulation of parallel-plate dielectric barrier discharge (DBD) using pure nitrogen and  $N_2/O_2$  gas driven by a realistic distorted-sinusoidal voltage power source (60 kHz) is studied. The simulated current-voltage characteristic results quantitatively agree with experimental measurements.

In the pure nitrogen simulations,  $N_4^+$  ion density is the dominant charged species, which is unlike most glow discharges. The discharge transforms from Townsend-like to filamentary-like (microdischarge) as gap distance is more than 1.0 mm, which was also observed in the experiment. All densities of charged and neutral species increase exponentially with increasing applied peak voltages in the range of 6.2-8.6 kV. The higher permittivity of the dielectric material is, the larger the discharge current and the longer the period of gas breakdown are. In addition, the quantity of accumulated charge at each electrode increases with increasing permittivity of the dielectric material. Finally, the increase of dielectric thickness from 1.0 to 2.0 mm greatly reduces the densities of all species and also the plasma absorbed power.

When trace amount of oxygen is introduced in nitrogen plasma, the dominate charged species are  $N_4^+$  and  $O_2^-$  with densities about  $10^{18} \text{ m}^{-3}$ . The neutral species

densities of  $N_2(A^3\Sigma_u^+)$  and atomic nitrogen are approximately  $4 \times 10^{19} \text{ m}^{-3}$  and  $1 \times 10^{21} \text{ m}^{-3}$  respectively, which agree well with experiments. The oxygen addition can significantly decrease the electron density from the order of  $10^{17} \text{ m}^{-3}$  down to  $10^{14} \text{ m}^{-3}$  as the fraction of trace oxygen increases from 0.003 % to 0.1 %. In addition, the calculated photon radiations are compared against the measured spectra. The spectral bands of second positive system (SPS) of  $N_2$ ,  $NO\gamma$ -system and  $ON_2$ -excimer are selected for comparison. Results reveal that the simulations and experiments show the similar trend with oxygen addition, in which the quantity of radiation increases rapidly first, peaks at some oxygen addition and then followed by a slow decrease.

Recommendations for future research are also outlined at the end of this thesis.



## 致 謝

在交大的求學過程，誠摯的感謝吳宗信教授在這幾年的諄諄教誨，您對學術的嚴謹和熱誠帶領著我們前進，並不時的為我們指引方向，在生活上非常照顧我們，在學習和生活上讓我獲益良多。同時也要感謝口試委員陳慶耀老師、徐振哲老師、魏大欽老師和陳彥升博士，謝謝您們在口試時提供的寶貴建議。另外特別感謝學長祭哥，不僅付出時間和心力教導我研究上的問題，同時也在我遇到許多困難時，給予我幫助與建議。

感謝實驗室的學長姐們，允民哥、周學姊、哲維兄、富利學長，也感謝實驗室的夥伴們，邱哥、阿孟、昆哥、江學長、雅茹、正勤兄、豪哥、古必、楊宜偉、劉志東、賴冠融、邱垂青、芳安、明忠等，與你們在一起相處的點點滴滴，一起在實驗室努力的時光，是我一生最寶貴的回憶。也感謝學弟妹們的大力幫忙，另外還有許多在生活或是學業上幫助我的人們或被不小心遺忘的朋友，在此也一併感謝，並祝福所有我的朋友們，能夠達到自己理想的目標。

最後要特別感謝我的家人，尤其是老爸與老媽，在我的求學生涯中從未間斷支持，這博士學位是父母親的成就。感謝他們對我的鼓勵與包容，在人生的旅途上我會更加努力向目標邁進。

鄭凱文 謹誌

2012年7月於交通大學

# Table of Contents

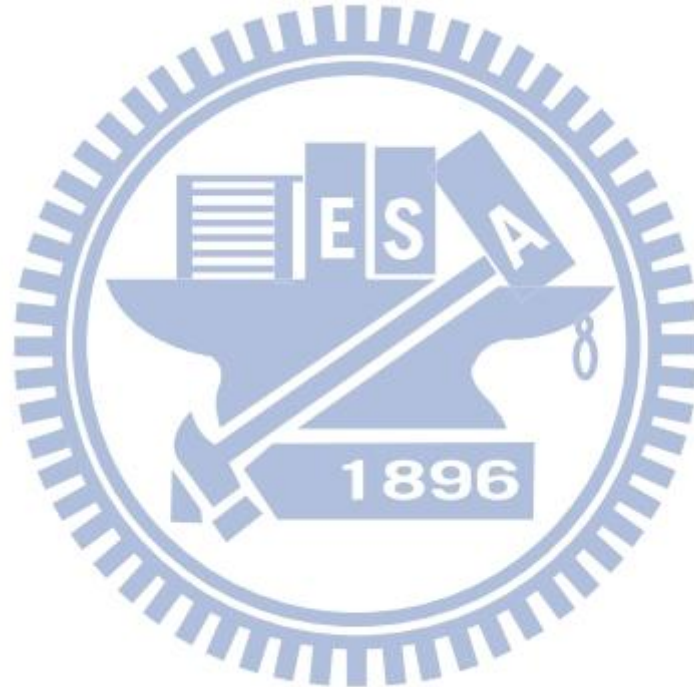
摘要.....	III
Abstract.....	V
致謝.....	VII
Table of Contents .....	VIII
List of Tables.....	X
List of Figures .....	XI
Nomenclature.....	XIII
Chapter 1 Introduction .....	1
1.1 Background and Motivation .....	1
1.1.1 Characteristics of the Plasma .....	1
1.1.1.1 Definition of Plasmas.....	1
1.1.1.2 Type of Plasmas .....	1
1.1.1.3 Applications of Plasmas.....	2
1.1.2 Characteristics of the Atmospheric Pressure Glow Discharge.....	3
1.1.3 Features of the Dielectric-Barrier Discharges (DBD).....	4
1.1.3.1 Structures .....	4
1.1.3.2 Advantages.....	4
1.1.3.3 Applications .....	5
1.2 Literature Survey .....	5
1.2.1 Atmospheric Pressure Dielectric-barrier Discharges.....	5
1.2.2 Simulations and Experiments on DBD with Pure Nitrogen .....	6
1.2.3 Simulations and Experiments on DBD with Nitrogen Mixed Oxygen .....	7
1.2.4 Numerical Approaches for Plasma Simulation.....	8
1.3 Specific Objectives of the Thesis.....	9
Chapter 2 Research Methods .....	11
2.1 Numerical Method of Fluid Modeling .....	11
2.1.1 Boltzmann Equation.....	11
2.1.2 Fluid Modeling Equations.....	12
2.2 Implementation of Semi-Implicit Scheme .....	15
2.3 Numerical Schemes and Discretization .....	17



2.4	Numerical Algorithm .....	21
2.5	Experimental Methods .....	22
2.6	Kinetic Model .....	23
Chapter 3 One-Dimensional Simulation of Nitrogen Dielectric Barrier Discharge Driven by a Quasi-pulsed Power Source and Its Comparison with Experiments.....		
3.1	Verification of the Fluid Modeling and Kinetic Model .....	26
3.2	Simulation Conditions .....	26
3.3	Basic Discharge Structure .....	27
3.4	Effect of Gap Distance .....	29
3.5	Effect of External Driving Voltage .....	30
3.6	Effect of Dielectric Material .....	31
3.7	Effect of Dielectric Thickness.....	32
Chapter 4 Numerical Investigation of Effects of Oxygen Addition on a Nitrogen-based Dielectric Barrier Discharge and Its Comparison with Experiments .		
4.1	Simulation Conditions .....	33
4.2	Basic Discharge Structure .....	33
4.4	Influence of Trace Oxygen on Cycle Average Properties .....	35
4.5	Influence of Trace Oxygen on Spectroscopic Properties .....	36
Chapter 5 Conclusion and Recommendations of Future Work.....		
5.1	Summary Remarks.....	37
5.2	Summary of Pure Nitrogen DBD Plasma .....	37
5.3	Summary of N <sub>2</sub> /O <sub>2</sub> DBD Plasma .....	38
5.4	Recommendations of Future Work .....	39
References.....		40
List of Publications .....		76

## List of Tables

Table 1: Subdivision of plasmas .....	44
Table 2: Nitrogen Plasma Chemistry .....	45
Table 3: N <sub>2</sub> /O <sub>2</sub> Plasma Chemistry .....	47
Table 4: Cycle average in different mesh number test.....	51
Table 5: Comparison of average absorbed power for varying applied voltage of 6200, 6600, 6800, 8600 V in a 60 kHz cycle, and a fixed gap distance of 0.5 mm.	52
Table 6: At 6200 V applied voltage and 60 kHz frequency, the compared of average number density, electron temperature and total absorbed power in different ceramic dielectric thickness (1.0 and 2.0 mm). .....	52

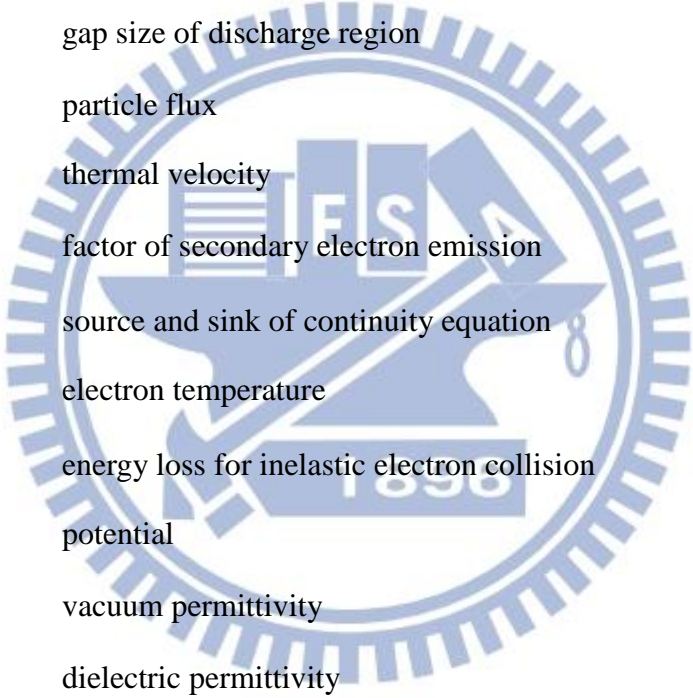


## List of Figures

Figure 1. 1: The frame work of background and motivation .....	53
Figure 1. 2: Sketch of dielectric barrier discharge .....	54
Figure 1. 3: The frame work of literature survey .....	55
Figure 2. 1: The frame work of research methods .....	56
Figure 2. 2: The flowchart of plasma fluid modeling .....	57
Figure 2. 3: Schematic sketch of a planar DBD APPJ .....	58
Figure 3. 1: The frame work of pure nitrogen results and discussions .....	59
Figure 3. 2: Comparison of simulated (upper) and [Gherardi's <i>et al.</i> , 2001] experimental (bottom) voltages and currents for atmospheric pressure discharge using sinusoidal 8 kHz power source. ....	60
Figure 3. 3: Comparison of simulated and experimented current-voltage characteristic with voltage 6600 V and frequency 60 kHz. The distance between the two dielectric layers is 0.5 mm and the dielectric is 2.0 mm alumina. The photo image of discharge acquired by 0.2 second exposed time was at the right. ....	61
Figure 3. 4: Distributions of various discharge currents during a cycle via numerical modeling. The gap distance is 0.5 mm and using 2.0 mm thickness alumina dielectric. The applied voltage is 6600 V and 60 kHz frequency. .....	62
Figure 3. 5: Distributions of various discharge currents at the maximum discharge current via numerical modeling. The gap distance is 0.5 mm and using 2.0 mm thickness alumina dielectric. The applied voltage is 6600 V and 60 kHz frequency.....	63
Figure 3. 6: Spatial distributions of electric field, charged particles and electron energy density at the time of maximum discharge current (0.86 $\mu$ s) between two alumina dielectric. The operating conditions are the same as in Figure 3. 3. ....	64
Figure 3. 7: Spatial distributions of electric field, charged particles and electron energy density at 15.5 $\mu$ s (after the breakdown) between two alumina dielectric. The operating conditions are the same as in Figure 3. 2.....	65
Figure 3. 8: Comparison of different gap distance (a) 0.5 mm (b) 0.7 mm (c) 1.0 mm (d) 1.4 mm discharged currents along with photo images of discharge at the right. ....	66
Figure 3. 9: Cycle-space averaged number densities of various species in nitrogen DBD for varying applied voltage of 6200, 6600, 6800, 8600 V, and a	

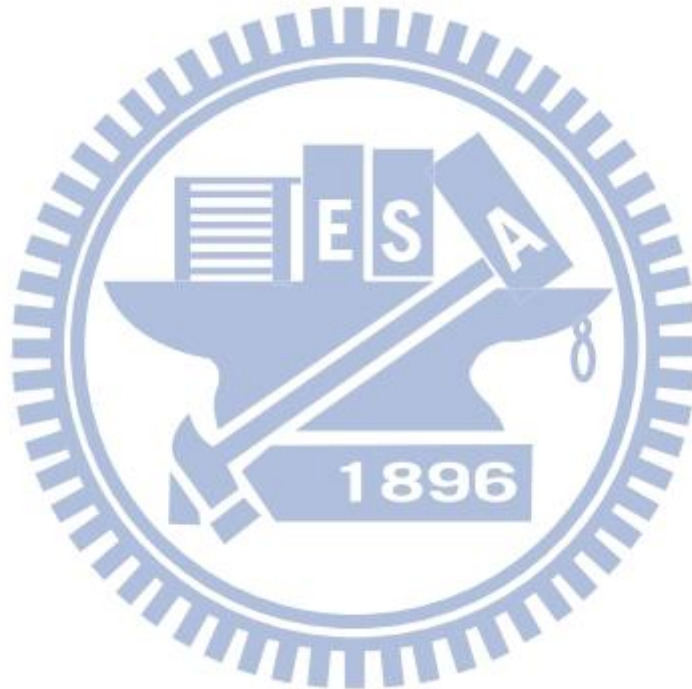
fixed gap distance of 0.5 mm. The alumina dielectric thickness is 2.0 mm and frequency is 60 kHz for all cases. ....	67
Figure 3. 10: Simulated current, gap voltage, applied voltage and accumulated charges at dielectric surfaces using 2.0 mm ceramic. The applied peak voltage is 8600 V and frequency is 60 kHz. The gap distance between dielectric is kept 0.5 mm. ....	68
Figure 3. 11: Simulated current, gap voltage, applied voltage and accumulated charges at dielectric surfaces using 2.0 mm quartz. The applied peak voltage is 8600 V and frequency is 60 kHz. The gap distance between dielectric is kept 0.5 mm. ....	69
Figure 4. 1: The frame work of oxygen addition on nitrogen-based results and discussions .....	70
Figure 4. 2: Comparison of simulated and experimented of N <sub>2</sub> with 0.03% O <sub>2</sub> current-voltage characteristic with voltage 8200 V and frequency 60 kHz. The distance between the two dielectric layers is 1.0 mm and the dielectric is 1.0 mm quartz.....	71
Figure 4. 3: Distributions of various spatial-average densities for charge species in N <sub>2</sub> + 0.03% O <sub>2</sub> DBD. The applied peak voltage is 8200 V and frequency is 60 kHz. The gap distance between quartz dielectric is 1.0 mm.....	72
Figure 4. 4: Distributions of various spatial-average densities for neutral species in N <sub>2</sub> + 0.03% O <sub>2</sub> DBD. The applied peak voltage is 8200 V and frequency is 60 kHz. The gap distance between quartz dielectric is 1.0 mm.....	73
Figure 4. 5: Cycle-space averaged number densities of various admixtures of oxygen (from 0.003% to 0.1%) in nitrogen DBD, and a fixed gap distance of 1.0 mm. The quartz dielectric thickness is 1.0 mm and frequency is 60 kHz for all cases. ....	74
Figure 4. 6: The calculated radiations (full curves) and experimental optical emission spectrums (dashed curves) were compared as a function of the trace oxygen. The spectral bands of SPS of N <sub>2</sub> , NO $\gamma$ -system and ON <sub>2</sub> -excimer were selected.....	75

## Nomenclature



$m$	mass
$P$	pressure
$q$	charge
$k_B$	the Boltzmann constant
$n$	number density
$l$	thickness of dielectric barrier
$L$	gap size of discharge region
$\Gamma$	particle flux
$v_{th}$	thermal velocity
$\gamma$	factor of secondary electron emission
$S$	source and sink of continuity equation
$T_e$	electron temperature
$\varepsilon$	energy loss for inelastic electron collision
$\phi$	potential
$\varepsilon_0$	vacuum permittivity
$\varepsilon_d$	dielectric permittivity
$E$	electric field
$f$	electron energy distribution function
$\sigma$	cross section
$k$	reaction rate coefficient
$\mu$	mobility
$D$	diffusivity
$\nu_m$	momentum exchange collision frequency between electron and background neutral particles

$\alpha$	polarizability
$\Delta x$	space interval
$\Delta t$	time interval
$B$	Bernoulli function



# Chapter 1 Introduction

## 1.1 Background and Motivation

A frame work of the background and motivation is revealed in [Figure 1. 1](#). Three categories of basic concept for plasma are introduced: characteristics of the plasma, characteristics of the atmospheric pressure glow discharge and features of the dielectric-barrier discharges.

### 1.1.1 Characteristics of the Plasma

The term "plasma" was coined by Irving Langmuir in 1928, who was the pioneers in gas discharges and defined plasma to be a region containing balanced charges of ions and electrons not influenced by its boundaries.

#### 1.1.1.1 Definition of Plasmas

The plasma state is often referred to as the fourth state of matter. It is distinct from other lower-energy states of matter; most commonly solid, liquid, and gas. Much of the visible matter in the universe is in the plasma state.

A plasma is a collection of free charged particles moving in random directions that is, on the average, electrically neutral. Plasmas are ionized gases. Hence, they consist of positive (and negative) ions and electrons, as well as neutral species. The ionization degree can vary from 100% (fully ionized gases) to very low values (e.g.  $1e-4$ ~ $1e-6$ ; partially ionized gases).

#### 1.1.1.2 Type of Plasmas

We can distinguish two main groups of plasma in [Table 1](#), i.e. the

high-temperature plasmas and the so-called low-temperature plasmas. Further, based on the relative temperatures of the electrons, ions and neutrals, low-temperature plasmas are classified as "thermal" or "non-thermal". Thermal plasmas have electrons and the heavy particles at the same temperature, i.e., they are in thermal equilibrium with each other. Non-thermal plasmas on the other hand have the ions and neutrals at a much lower temperature. Because of the large difference in mass, the electrons come to thermodynamic equilibrium amongst themselves much faster than they come into equilibrium with the ions or neutral atoms. For this reason, the "ion temperature" may be very different from (usually lower than) the "electron temperature". This is especially common in weakly ionized technological plasmas, where the ions are often near the ambient temperature.

### **1.1.1.3 Applications of Plasmas**

Plasmas have been utilized in many well-established industrial applications (e.g. for surface modification, lasers, lighting, among others). In the following, we will describe some of the most widespread applications:

First, surface treatment and modification with the possibility to treat (and to coat) a surface at low temperature and at pressure close to atmospheric is an important advantage for industrial applications. The operating gases included air, He, N<sub>2</sub>, N<sub>2</sub> + O<sub>2</sub>, Ar, CF<sub>4</sub>, NH<sub>3</sub>, Cl<sub>2</sub>, etc. Second, ozone is a potent germicide and one of the strongest known oxidants. The main applications of ozone generation are in water treatment (drinking water plants using ozone for disinfection) and in pulp bleaching. The operating gases include dried clean air or dry oxygen. Third, plasma is used to provide reactive species such as N<sub>2</sub><sup>\*</sup>, O<sub>2</sub><sup>\*</sup>, O(<sup>1</sup>D), O(<sup>3</sup>P), N(<sup>4</sup>S) in pollution control applications. These species initially formed by electron collisions in the microdischarge filaments subsequently provide a number of reaction paths to generate



additional O and OH. These radicals can subsequently react with hazardous compounds to form non-hazardous or less hazardous substances such as O<sub>2</sub>, O<sub>3</sub>, CO, CO<sub>2</sub>, H<sub>2</sub>O<sub>2</sub>. Fourth, gas discharges are also used for laser applications, more specifically as gas lasers (e.g. high speed welding and cutting of metal plates and other materials is the main application of silent discharge CO<sub>2</sub> laser). Fifth, The lamps especially used for high-speed printing on heat sensitive substrates. Large numbers of xenon excimer lamps are now routinely used for “UV cleaning” of substrates in display and semiconductor manufacturing. Finally, plasma display panels (PDPs) displays utilizing Xe VUV radiation to excite phosphors are the most recent addition to dielectric-barrier discharge applications.

### **1.1.2 Characteristics of the Atmospheric Pressure Glow Discharge**

When the applied voltage exceeds the breakdown strength of the ambient gas, an avalanche is formed. During the short breakdown period, the non-conducting gas becomes conductive and, as a result, generates different kinds of plasmas. The understanding of kinetic processes in plasmas of atmospheric gases is of great interest in various branches of modern physics and chemistry, such as discharge physics, plasma chemistry, chemistry and optics of the atmosphere. In order to get the appropriate plasma parameters, the experimental and theoretical investigations are quite important tools for understanding the plasma properties.

The measurements in a discharge at atmospheric pressure are related to light intensity (spectroscopic measurements and short exposure time photo) and electrical characteristics (measurements of the discharge current and construction of the Lissajous figures). But spectroscopic or electric diagnostics have the limitation in the investigations of discharge behavior such as distribution of electric field and plasma particle density over discharge gap. Recently, simulation has become an important

method in understanding the plasma physics and chemistry of gas discharges since the direct quantitative measurements inside the discharge volume are either very difficult or very costly. Not only can an efficient and accurate modeling provide detailed plasma physics and chemistry within complex gas discharges, but also may it be used as an optimization tool for designing a new plasma source.

### **1.1.3 Features of the Dielectric-Barrier Discharges (DBD)**

#### **1.1.3.1 Structures**

A sketch of dielectric barrier discharge is showed [Figure 1. 2](#). The DBD usually is generated in the space between two electrodes covered with the insulating dielectric material. The most frequently used dielectric materials being Pyrex, quartz, polymers and ceramics, in some applications additional protective or functional coatings are applied. When the applied voltage exceeds the breakdown strength of the ambient gas, an avalanche is formed. Sources that operate under vacuum are at a disadvantage with respect to those that operate at 1 atm because of the increased capital costs and the requirement for batch processing of workpieces associated with vacuum systems.

#### **1.1.3.2 Advantages**

Types of non-equilibrium atmospheric-pressure plasma (APP) are generally classified based on the power sources, which may include radio frequency (RF) capacitively coupled discharge, AC dielectric barrier discharge (DBD) and microwave discharge. Among these, the parallel-plate DBD driven by AC power supply (10-100 kHz) may represent one of the most attractive discharges because of: 1) its easier implementation as compared with low-pressure plasmas, 2) low operational cost 3) possibility of the production of homogeneous plasma, 4) lower working temperature.

### 1.1.3.3 Applications

Dielectric-barrier discharges, or simply barrier discharges, have been known for more than a century. First experimental investigations were reported in 1857. The DBD at atmospheric pressure driven by a alternating current power source has been widely used in various industrial fields, such as surface treatment, thin film deposition, pollution control, plasma display cell production. The DBD is generated in the space between two electrodes, which were covered with insulating dielectric layers.

## 1.2 Literature Survey

Recently, atmospheric-pressure plasma (APP) has attracted considerable attention, mainly because, unlike low-pressure plasmas, APP does not require the use of vacuum equipment and it is increasingly used in modern science and technology applications. In the following we focus on introducing the AP DBD literature surveys which are restricted along this line. A frame work of the literature survey is revealed in [Figure 1.3](#).

### 1.2.1 Atmospheric Pressure Dielectric-barrier Discharges

Dielectric-barrier discharges, or simply barrier discharges, have been known for more than a century. First experimental investigations were reported by Siemens in 1800s [Kogelschatz, 2003]. DBD used in the industry usually operate at 1 atm, therefore we focus the plasma in the atmospheric operating pressure. Depending on discharge conditions and geometry, the DBD may appear in two discharge forms: homogeneous and filamentary.

The filamentary discharge consists of a large number of narrow (about 100 $\mu$ m) filaments stochastically distributed over the electrode area. The discharge current has

the form of multiple peaks (microdischarges), about 10 ns in duration. There is a large number of works where filamentary discharge (a most common form of the DBD) has been simulated, for example [Papageorghiou *et al.*, 2009]. Most of the works are devoted to the study of a single microdischarge on the basis of a fluid model.

Under certain conditions (for example, frequency and applied voltage...), DBD is homogeneous along the plane of the electrodes. The homogeneous discharge allows one to treat surfaces more uniformly. The homogeneous barrier discharge was obtained in helium [Massines *et al.*, 1998; Mangolini *et al.*, 2002], neon [Trunec *et al.*, 2001], nitrogen [Tepper *et al.*, 2000; Sègur *et al.*, 2000], air [Tepper *et al.*, 2000] and other gases. The homogeneous discharge is realized in two forms: Townsend and glow discharge.

The glow form (atmospheric pressure glow discharge) is characterized by higher discharge current (hundreds of milliamperes) and abrupt alteration of the electric field in the discharge gap. On the contrary, the discharge current in the Townsend discharge is much smaller (units of milliamperes) and the electric field is practically homogeneous along the discharge axis. This Townsend of the homogeneous discharge was observed in most working gases [Mangolini *et al.*, 2002; Tepper *et al.*, 2000; Mangolini *et al.*, 2002]. In the present research, we take nitrogen as the working gas, because the homogeneous barrier discharge in nitrogen appears mostly as a Townsend discharge.

## **1.2.2 Simulations and Experiments on DBD with Pure Nitrogen**

A Townsend-like barrier discharge in nitrogen at 7 kHz frequency and sinusoidal voltage is studied experimentally and theoretically by [Golubovskii *et al.*, 2006]. The experimental results are compared with the calculations of the existence range of barrier discharges in different forms, which were performed on the basis of a fluid

model. The influences of the barrier material and thickness are discussed while the permittivity of dielectric is 2.2-8.0 and thickness of dielectric from 1.0 to 2.0 mm. It is shown that the lower the permittivity of barriers is, the wider is the range of parameters where the discharge is homogeneous. However, it is considered in this thesis that the effects of permittivity in the more high frequencies higher than 60 kHz with realistic distorted sinusoidal AC power source.

The properties of a barrier discharge in nitrogen near the transition from the Townsend mode to the filamentary mode are studied on the basis of a two dimensional fluid model by [Maiorov *et al.*, 2007]. It is shown that the widening of the stability region for the discharge with small gap distance is proved. Therefore, in the thesis considered the effects of gap distance in the more high frequency 60 kHz with realistic distorted sinusoidal AC power source.

An one-dimension fluid model for pure nitrogen atmospheric pressure plasma was studied [Choi *et al.*, 2006]. The influences of different driving frequencies and voltage amplitudes are discussed while the amplitude of sinusoidal applied voltage is 6-10 kV and frequency changes from 10 to 20 kHz. The increase of the amplitude and frequency of external voltage lead to the increase of plasma density. In addition, the dielectric constants of the barrier materials have also shown a strong influence on the discharge structure. The simulation of pure nitrogen barrier discharge and the nitrogen with different content of oxygen are presented.

### **1.2.3 Simulations and Experiments on DBD with Nitrogen Mixed Oxygen**

The nitrogen with small admixtures of oxygen barrier discharge at frequency of 6.95 kHz was studied [Brandenburg *et al.*, 2005]. The electric characteristics with different external admixture of O<sub>2</sub> and the spectroscopic diagnostics are measured

from experiment, and the discharge current and displacement current are compared with numerical and experiment results. The transition to the filamentary mode and the discharge mechanism are discussed, this transition starts from less of oxygen (about 450 ppm) to the micro-discharges, which are generated at higher admixtures of O<sub>2</sub> (about 1000 ppm).

The techniques of spatially resolved cross-correlation spectroscopy (CCS) and current pulse oscillography were used to carry out systematic investigations of the barrier discharge (BD) by [Kozlov *et al.*, 2005]. Under the experimental conditions being considered (symmetrical electrode configuration ‘glass–glass’, gap width of about 1 mm, feeding voltage frequency of 6.5 kHz), in the binary N<sub>2</sub>/O<sub>2</sub> mixtures at atmospheric pressure. Special attention was devoted to the investigation of the transition between the filamentary and diffuse modes of the BD, this transition being caused by the variation of oxygen content within the range 500–1000 ppm. The spatio-temporal distributions of the filamentary BD radiation intensities were recorded for the spectral bands of the 0–0 transitions of the second positive ( $\lambda = 337$  nm) and first negative system of molecular nitrogen ( $\lambda = 391$  nm). In the case of the diffuse mode, the spectral bands  $\lambda = 337$  nm,  $\lambda = 260$  nm (0–3 transition of the  $\gamma$ -system of NO) and  $\lambda = 557$  nm (radiation of ON<sub>2</sub> excimer) were used in the paper.

#### **1.2.4 Numerical Approaches for Plasma Simulation**

Generally speaking, there are four different types of approaches to plasma simulation, which can be applied in different plasma conditions. They include: (1) direct Boltzmann equation solver, (2) Particle-in-Cell with Monte-Carlo collision method (PIC-MCC), (3) fluid modeling, and (4) hybrid fluid-PIC method. We are only focus in fluid modeling as following in turn.

Fluid model of plasma is based on partial differential equations which describe

the macroscopic quantities such as density, flux, average velocity, pressure, temperature or heat flux. The governing equations can be derived from the Boltzmann equation by taking velocity moments of the Boltzmann equation with some assumptions [Meyyappan, 1994; Gogolides *et al.*, 1992; Pitaevskii *et al.*, 1981] including the continuity equation, momentum equation and energy equation. The fluid descriptions break down for highly rarefied plasma, or intense nonlocal effect induced by strongly electric field. Related publications of fluid modeling could be found in numerous articles, e.g. [Ventzek *et al.*, 1993; LyMBERopoulos *et al.*, 1995; Bukowski *et al.*, 1996], and are not reported here.

There are generally two types of fluid modeling techniques: (1) local field approximation (LFA) and (2) local-mean-energy approximation (LMEA). The former assumes the input electric power into the plasma is fully balanced by the power dissipated by ionization, while the latter solves the electron energy density equation directly. Although the transport and rate coefficients of electrons are obtained from the solution of stationary spatially homogeneous Boltzmann equation, the consequences are quite different. It has been shown that the use of LMEA is generally much better than the LFA because of the former considers non-local effect of electron energy distributions [Grubert *et al.*, 2009].

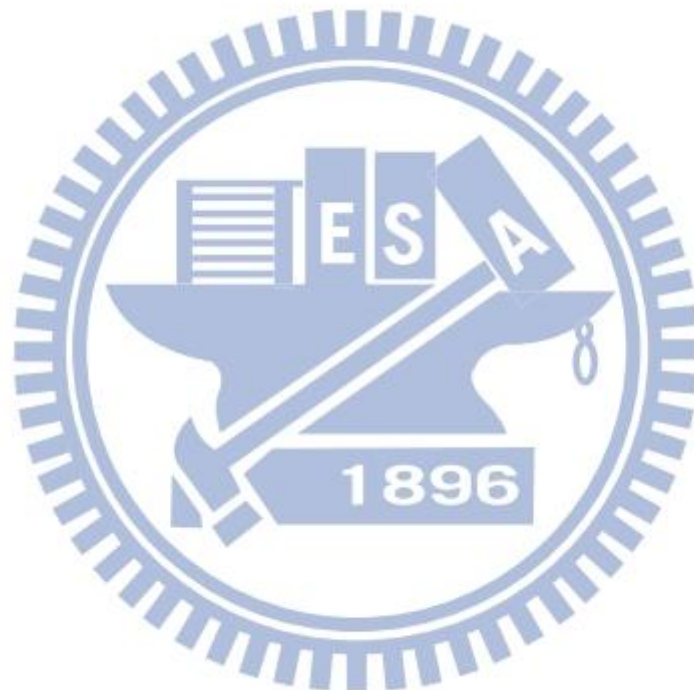
### **1.3 Specific Objectives of the Thesis**

Understanding of the plasma physics and chemistry employed in low-temperature plasma applications has been generally difficult through experimental measures. Therefore, numerical simulations are used to study the atmospheric nitrogen and  $N_2/O_2$  plasma. The specific objectives of this thesis are summarized as follows,

1. To simulate a 1-D nitrogen dielectric barrier discharge at atmospheric pressure

and compare the numerical result with experiment data.

2. To discuss the effects of operated parameter (applied voltage, dielectric material, dielectric thickness, gap distance...) in nitrogen plasma and its physics.
3. To study the effects of trace oxygen in nitrogen plasma with various amounts and to compare with experimental data.





## Chapter 2 Research Methods

A frame work of the research methods are revealed in [Figure 2. 1](#). Three distinct components for studying atmospheric pressure dielectric barrier discharge are introduced: numerical method of fluid modeling, experimental methods and kinetic model.

### 2.1 Numerical Method of Fluid Modeling

#### 2.1.1 Boltzmann Equation

According to kinetic theory, the plasma can be described by a distribution function  $f(\mathbf{r}, \mathbf{v}, t)$ , which satisfies the Boltzmann equation (Vlasov equation), at location  $\mathbf{r}$ , velocity  $\mathbf{v}$  and time  $t$ ,

$$\frac{\partial}{\partial t} f(\mathbf{r}, \mathbf{v}, t) + \mathbf{v} \cdot \nabla_{\mathbf{r}} f(\mathbf{r}, \mathbf{v}, t) + \frac{q}{m} (\mathbf{E} + \mathbf{v} \times \mathbf{B}) \cdot \frac{\partial f(\mathbf{r}, \mathbf{v}, t)}{\partial \mathbf{v}} = \left( \frac{\partial f(\mathbf{r}, \mathbf{v}, t)}{\partial t} \right)_c$$

, where  $q$  is charge,  $m$  is mass, and the term in right hand side is due to collision. If we take the first three velocity moments of  $f(\mathbf{r}, \mathbf{v}, t)$ , the spatial and temporal distribution of density, flux, and temperature can be described as

$$n(\mathbf{r}, t) = \int f(\mathbf{r}, \mathbf{v}, t) d^3 \mathbf{v}$$

$$\Gamma(\mathbf{r}, t) = \int \mathbf{v} f(\mathbf{r}, \mathbf{v}, t) d^3 \mathbf{v}$$

$$\frac{3}{2} k_B T(\mathbf{r}, t) = \frac{m}{2} \frac{\int v^2 f(\mathbf{r}, \mathbf{v}, t) d^3 \mathbf{v}}{\int f(\mathbf{r}, \mathbf{v}, t) d^3 \mathbf{v}}$$

Similarity, we take the three previous integrations of Boltzmann equation to get the continuity equation, momentum equation and energy equation, these equations can

be written as,

$$\begin{aligned}\frac{\partial}{\partial t} n + \nabla \cdot (nv) &= S \\ mn \left[ \frac{\partial v}{\partial t} + (v \cdot \nabla)u \right] &= qn(E + v \times B) - \nabla \cdot P + M \\ \frac{\partial}{\partial t} (nC_v T) + \nabla \cdot (nC_v T) &= -\nabla \cdot q - p \nabla \cdot v + E\end{aligned}$$

, where  $S$  is the source and sink of the continuity equation,  $M$  is the momentum transfer of the species,  $E$  is the energy gain and loss of the species,  $C_v$  is the specific heat capacity.

## 2.1.2 Fluid Modeling Equations

In general fluid modeling, the densities of electron, ion and neutral species are function of time and space, which are calculating from the species continuity equations, species momentum equations and species energy equations. Further, the self-consistent model includes the Poisson's equation.

Transport coefficients, mobility and diffusivity, are used instead of solving species momentum equations, and ignoring the ionic and neutral species energy equations because of the non-thermal plasma is considered. Therefore, only species continuity equations, electron energy equation and Poisson's equation are solved.

The general continuity equation for ion species can be written as

$$\frac{\partial n_p}{\partial t} + \frac{\partial \Gamma_p}{\partial x} = \sum_{i=1}^{r_p} S_{pi} \quad , \quad p = 1, 2, \dots, k \quad (1)$$

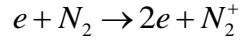
where  $n_p$  is the number density of ion species  $p$ ,  $k$  is the number of ion species,  $r_p$  is the number of reaction channels that involve the creation and destruction of ion species  $p$ , and  $\vec{\Gamma}_p$  is the ion particle flux that is expressed as, base on the drift-diffusion approximation,

$$\Gamma_p = \text{sign}(q_p) \mu_p n_p E - D_p \frac{\partial n_p}{\partial x} \quad (2)$$

where  $q_p$ ,  $\mu_p$ , and  $D_p$  are the ion charge, the ion mobility, and the ion diffusivity of the species  $p$ . The electric field  $E$  can be calculated by the potential  $\phi$  as

$$E = -\frac{\partial\phi}{\partial x} \quad (3)$$

The source term  $S$  is calculated from the chemistry reactions, for example, there is a reaction channel which reaction rate is  $k_i$  as following,



Therefore, the source term of  $N_2^+$  can be written as,

$$S_i = k_i n_e n_{N_2} \quad (4)$$

The continuity equation for electron species  $e$  can be written as

$$\frac{\partial n_e}{\partial t} + \frac{\partial \Gamma_e}{\partial x} = \sum_{i=1}^{r_e} S_{ei} \quad (5)$$

where  $n_e$  is number density of electron,  $r_e$  is the number of reaction channels that involve the creation and destruction of electron, and  $\vec{\Gamma}_e$  is the electron particle flux that is expressed as, base on the drift-diffusion approximation,

$$\Gamma_e = \text{sign}(q_e) \mu_e n_e E - D_e \frac{\partial n_e}{\partial x} \quad (6)$$

where  $\mu_e$  and  $D_e$  are the electron mobility and electron diffusivity, respectively. These two transport coefficients can be readily obtained as a function of the electron temperature from the solution of a publicly available computer code for the Boltzmann equation, named BOLSIG+ [Balay *et al.*, 2001]. Similar to  $S_p$ , the form of  $S_{ei}$  can also be modified according to the modeled reactions that generate or destroy the electron in reaction channel  $i$ . The boundary conditions at the walls are applied considering the thermal diffusion, drift and diffusion fluxes which can be represented as

$$\Gamma_e = \text{sign}(q_e)\mu_e n_e E - D_e \frac{\partial n_e}{\partial x} + \frac{1}{4} n_e \sqrt{\frac{8k_B T_e}{\pi m_e}} - \gamma \sum \Gamma_i \quad (7)$$

where  $k_B$  is Boltzmann constant,  $m_e$  is the mass of electron, and  $\gamma$  is the electron emission coefficient.

The continuity equation for neutral species can be written as

$$\frac{\partial n_{uc}}{\partial t} + \frac{\partial \Gamma_{uc}}{\partial x} = \sum_{i=1}^{r_{uc}} S_{uc,i}, \quad uc = 1, 2, \dots, k \quad (8)$$

where  $n_{uc}$  is number density of electron,  $r_{uc}$  is the number of reaction channels that involve the creation and destruction of neutral species  $uc$ , and  $\vec{\Gamma}_e$  is the particle flux only considering the diffusion effect,

$$\Gamma_{uc} = -D_{uc} \frac{\partial n_{uc}}{\partial x} \quad (9)$$

where  $D_{uc}$  is the diffusivity of neutral species. Similarly, the form of  $S_{uc,i}$  can also be modified according to the modeled reactions that generate or destroy the species in reaction channel  $i$ . Neumann boundary conditions at walls are applied to neutral species fluxes.

The electron energy density equation can be written as,

$$\frac{\partial n_\varepsilon}{\partial t} + \frac{\partial \Gamma_\varepsilon}{\partial x} = -e\Gamma_e E - \sum_{i=1}^{S_c} \varepsilon_i S_i + 3 \frac{m_e}{M} n_e k_B \nu_m (T_e - T_g) \quad (10)$$

where  $T_e$  is the electron temperature,  $T_g$  is the background gas temperature,  $\varepsilon_i$  is the energy loss for  $i^{\text{th}}$  inelastic electron collision,  $k_B$  is Boltzmann constant, and  $\nu_m$  is the momentum exchange collision frequency between electron and background neutral particles.  $n_\varepsilon$  is the electron energy density which is defined as

$$n_\varepsilon = \frac{3}{2} n_e k_B T_e \quad (11)$$

The electron energy density flux  $\vec{\Gamma}_\varepsilon$  is

$$\Gamma_\varepsilon = \frac{5}{2} k_B T_e \Gamma_e - \frac{5}{2} \frac{n_e k_B T_e}{m_e \nu_m} \nabla(k_B T_e) \quad (12)$$

The second term on the right-hand side of Eq. (10) represents the sum of the energy losses of the electrons due to inelastic collision with other species. The last term on the right-hand side of Eq. (10) can be ignored for low-pressure gas discharges, while it is important for medium-to-atmospheric pressure discharges. The boundary conditions of electron energy density fluxes can be represented as

$$\vec{\Gamma}_{n_e} = 2T_e\vec{\Gamma}_e \quad (13)$$

Poisson's equation can be written as,

$$\frac{\partial^2 \phi}{\partial x^2} = -\frac{1}{\varepsilon_0} \left( \sum_{i=1}^k (\text{sign}) q_i n_i - en_e \right) \quad (14)$$

where  $\varepsilon_0$  is the vacuum permittivity.

## 2.2 Implementation of Semi-Implicit Scheme

It was reported that explicit evaluation of source term of Poisson equation leads to small time step to avoid numerical instability due to the restriction of dielectric relaxation time which can be represented as [Ventzek *et al.*, 1993]

$$\Delta t < t_{dielectric} = \frac{\varepsilon_0}{\sum_p |q| \mu_p n_p} \quad (15)$$

This instability is caused by the use of number density of previous time step to calculate the source term of Poisson equation since there is no number density of current time step while solving Poisson equation. The so called semi-implicit treatment is applied on the source term of Poisson equation to ensure stability. The predicted source term of current time step of Poisson equation is linearized with a Taylor-series expansion in time as

$$\left(\sum_{i=1}^K q_i n_i - en_e\right)^{k+1} \approx \left(\sum_{i=1}^K q_i n_i - en_e\right)^k + \Delta t \left( \frac{d \left( \sum_{i=1}^K q_i n_i - en_e \right)}{dt} \right)^k \quad (16)$$

where  $n_e$  represents the number density of electron, and  $n_i$  represents the number density of ions. The temporal gradient of number density of species can be calculated from continuity equation of each species. With some derivations and approximations, the Poisson equation can be written as

$$\nabla^2 \phi = -\frac{1}{\epsilon_0} \left( \sum_{i=1}^K q_i n_i - en_e \right) \left( 1 + \frac{\Delta t}{\epsilon_0} \left( \sum_{i=1}^K \mu_i n_i - \mu_e n_e \right) \right) \quad (17)$$

Similar constraint on time step size can be found on the source term of the electron energy density equation, Eq. (10), and the energy source term is linearized by a Taylor's series expansion in electron energy with some approximations for increasing the time step size of the simulation [Hagelaar *et al.*, 2000]. Thus, the electron energy density equation can be rewritten as

$$\begin{aligned} \frac{\partial n_e}{\partial t} + \nabla \cdot \vec{\Gamma}_{n_e} = & -e \left( \vec{\Gamma}_e \cdot \vec{E} \right)^k - \left( n_e \sum_{i=1}^{s_e} \epsilon_i k_i n_i \right)^k - \left( 3 \frac{m_e}{M} n_e k_B v_m (T_e - T_g) \right)^k \\ & - \left[ \frac{e}{n_e} \vec{E} \cdot \frac{\partial \vec{\Gamma}_e}{\partial \mu_e} \frac{\partial \mu_e}{\partial \bar{\epsilon}} + \frac{e}{n_e} \vec{E} \cdot \frac{\partial \vec{\Gamma}_e}{\partial D_e} \frac{\partial D_e}{\partial \bar{\epsilon}} + \sum_{i=1}^{s_e} \epsilon_i \frac{\partial k_i}{\partial \bar{\epsilon}} n_i + 3 \frac{m_e}{M} k_B \frac{\partial v_m}{\partial \bar{\epsilon}} (T_e - T_g) \right]^k \left( n_e^{k+1} - n_e^{k+1} \bar{\epsilon}^k \right) \end{aligned} \quad (18)$$

The discretization form of  $\frac{\partial \vec{\Gamma}_e}{\partial \mu_e} \frac{\partial \mu_e}{\partial \bar{\epsilon}} + \frac{\partial \vec{\Gamma}_e}{\partial D_e} \frac{\partial D_e}{\partial \bar{\epsilon}}$  has been derived based on the Scharfetter-Gummel (SG) scheme [Scharfetter *et al.*, 1969] in one-dimensional example as

$$\begin{aligned} \left( \frac{\partial \vec{\Gamma}_e}{\partial \mu_e} \frac{\partial \mu_e}{\partial \bar{\epsilon}} + \frac{\partial \vec{\Gamma}_e}{\partial D_e} \frac{\partial D_e}{\partial \bar{\epsilon}} \right)_{i+\frac{1}{2}} = & -\frac{2}{3e\Delta x} u_{e,i+\frac{1}{2}} h \left( z_{i+\frac{1}{2}} \right) \left( n_{e,i+1} - n_{e,i} \right) \\ & + \frac{1}{\mu_{e,i+\frac{1}{2}}} \left( \frac{\partial \mu_e}{\partial \bar{\epsilon}} \right)_{i+\frac{1}{2}} \Gamma_{e,i+\frac{1}{2}} \end{aligned} \quad (19)$$

where  $h(z) = \frac{z^2 \exp(z)}{(\exp(z)-1)^2}$ , and  $z = \frac{\text{sign}(q)\mu E \Delta x}{D}$ . Details of the implement can be found in references [Ventzek *et al.*, 1993; Hagelaar *et al.*, 2000], and are not described here for brevity.

### 2.3 Numerical Schemes and Discretization

The plasma fluid modeling is spatially discretized by finite volume method as the following two-dimensional general form

$$\frac{\partial \phi_{i,j}}{\partial t} + \frac{F_{i+1/2,j} - F_{i-1/2,j}}{\Delta x_{i,j}} + \frac{G_{i+1/2,j} - G_{i-1/2,j}}{\Delta y_{i,j}} = S_{i,j} \quad (20)$$

where  $\phi = \begin{bmatrix} n_p \\ n_e \\ n_{uc} \\ n_\varepsilon \end{bmatrix}$ ,  $F = \begin{bmatrix} \Gamma_p \\ \Gamma_e \\ \Gamma_{uc} \\ \Gamma_{n_\varepsilon} \end{bmatrix}_x$ ,  $G = \begin{bmatrix} \Gamma_p \\ \Gamma_e \\ \Gamma_{uc} \\ \Gamma_{n_\varepsilon} \end{bmatrix}_y$ ,  $\Delta x$  and  $\Delta y$  stand for cell width in x and y

direction of peculiar cell, and  $S_{i,j}$  stands for the corresponding source term. The Poisson equation is spatially discretized by similar manner with the flux term is calculated by central difference scheme as described later in this section, and those fluxes of continuity equations and electron energy density equation are calculated by SG scheme [Scharfetter *et al.*, 1969] as introduced below.

The SG scheme is one of the most popular numerical schemes for plasma simulation. The following derivation of SG scheme uses one-dimensional example for demonstration. It can be extended easily for two-dimensional problem. Consider a one-dimensional problem, the flux between cell  $i$  and  $i+1$  is denoted as  $\Gamma_{i+1/2}$  and can be written as

$$\Gamma_{p,i+1/2} = -D_{p,i+1/2} \frac{\partial n_p}{\partial x} - q\mu_{p,i+1/2} \frac{\partial \phi}{\partial x} n_p \quad (21)$$

where  $q = 1$  for ion with one positive charge and  $q = -1$  for electron or ion with one negative charge. To change the variable from position to potential, we apply chain rule to Eq. (21) and obtain

$$\frac{\partial n_p}{\partial \phi} \frac{\partial \phi}{\partial x} + \frac{q\mu_{p,i+1/2}}{D_{p,i+1/2}} \frac{\partial \phi}{\partial x} n_p = -\frac{\Gamma_{p,i+1/2}}{D_{p,i+1/2}} \quad (22)$$

We assume that  $\frac{\partial \phi}{\partial x}$  is independent of potential and divide both sides by  $\frac{\partial \phi}{\partial x}$ , then

we have

$$\frac{\partial n_p}{\partial \phi} + \frac{q\mu_{p,i+1/2}}{D_{p,i+1/2}} n_p = -\frac{\Gamma_{p,i+1/2}}{D_{p,i+1/2}} \frac{\partial \phi}{\partial x} \quad (23)$$

Eq. (23) is a non-homogeneous 1st order differential equation (ODE) with constant coefficients since we approximate the mobility and diffusivity with constants. The solution of a non-homogeneous ODE includes homogeneous and particular solution and could be represented as

$$n_p(\phi) = n_h(\phi) + n_{par}(\phi) = Ce^{\lambda\phi} - \frac{\Gamma_{p,i+1/2}}{q\mu_{p,i+1/2}} \frac{\partial \phi}{\partial x} \quad (24)$$

where  $\lambda = -\frac{q\mu_{p,i+1/2}}{D_{p,i+1/2}}$ . Substitute Eq. (24) into Eq. (23) with boundary conditions

$n_p(\phi_i) = n_{p,i}$  and  $n_p(\phi_{i+1}) = n_{p,i+1}$  to solve the constant and obtain

$$C = \frac{n_{p,i+1} - n_{p,i}}{e^{\lambda\phi_{i+1}} - e^{\lambda\phi_i}} \quad (25)$$

Hence, the flux can be represented as



$$\Gamma_{p,i+1/2} = \frac{-D_{p,i+1/2}}{x_{i+1} - x_i} \left[ \frac{\lambda(\phi_{i+1} - \phi_i)}{e^{\lambda(\phi_{i+1} - \phi_i)} - 1} n_{p,i+1} - \frac{-\lambda(\phi_{i+1} - \phi_i)}{e^{-\lambda(\phi_{i+1} - \phi_i)} - 1} n_{p,i} \right] \quad (26)$$

where the potential gradient can be approximated with finite difference method as

$$\frac{\partial \phi}{\partial x} = \frac{\phi_{i+1} - \phi_i}{x_{i+1} - x_i} \quad (27)$$

Finally, the flux can be represented as

$$\Gamma_{p,i+1/2} = \frac{-D_{p,i+1/2}}{x_{i+1} - x_i} [B(-X)n_{p,i+1} - B(X)n_{p,i}] \quad (28)$$

where  $X = -\lambda(\phi_{i+1} - \phi_i) = \frac{q\mu_{p,i+1/2}}{D_{p,i+1/2}}(\phi_{i+1} - \phi_i)$  and  $B$  is the Bernoulli function as

$$B(X) = \frac{X}{e^X - 1} \quad (29)$$

Thus, the flux of each cell can be evaluated with SG scheme and complete the finite volume method.

The complete form of continuity equation can be written as

$$\begin{aligned} \frac{\partial n_{i,j}}{\partial t} + \frac{\partial \Gamma_{i,j}}{\partial x} + \frac{\partial \Gamma_{i,j}}{\partial y} &= S_{i,j} \\ \Rightarrow \frac{n_{i,j}^{k+1} - n_{i,j}^k}{\Delta t} + \frac{\Gamma_{i+1/2,j}^{k+1} - \Gamma_{i-1/2,j}^{k+1}}{\Delta x_{i,j}} + \frac{\Gamma_{i,j+1/2}^{k+1} - \Gamma_{i,j-1/2}^{k+1}}{\Delta y_{i,j}} &= S_{i,j}^k \end{aligned} \quad (30)$$

where

$$\Gamma_{i+1/2,j}^{k+1} = -\frac{D_{i+1/2,j}^k}{x_{i+1,j} - x_{i,j}} \left[ B(-X_{i+1/2,j}) n_{i+1,j}^{k+1} - B(X_{i+1/2,j}) n_{i,j}^{k+1} \right]$$

$$\Gamma_{i-1/2,j}^{k+1} = -\frac{D_{i-1/2,j}^k}{x_{i,j} - x_{i-1,j}} \left[ B(-X_{i-1/2,j}) n_{i,j}^{k+1} - B(X_{i-1/2,j}) n_{i-1,j}^{k+1} \right]$$

$$\Gamma_{i,j+1/2}^{k+1} = -\frac{D_{i,j+1/2}^k}{y_{i,j+1} - y_{i,j}} \left[ B(-X_{i,j+1/2}) n_{i,j+1}^{k+1} - B(X_{i,j+1/2}) n_{i,j}^{k+1} \right]$$

$$\Gamma_{i,j-1/2}^{k+1} = -\frac{D_{i,j-1/2}^k}{y_{i,j} - y_{i-1,j}} \left[ B(-X_{i,j-1/2}) n_{i,j}^{k+1} - B(X_{i,j-1/2}) n_{i,j-1}^{k+1} \right]$$

$$X_{i+\frac{1}{2},j} = -\frac{q\mu_{i+\frac{1}{2},j}^k}{D_{i+\frac{1}{2},j}^k}(\phi_{i+1,j} - \phi_{i,j})$$

$$X_{i-\frac{1}{2},j} = -\frac{q\mu_{i-\frac{1}{2},j}^k}{D_{i-\frac{1}{2},j}^k}(\phi_{i,j} - \phi_{i-1,j})$$

$$X_{i,j+\frac{1}{2}} = -\frac{q\mu_{i,j+\frac{1}{2}}^k}{D_{i,j+\frac{1}{2}}^k}(\phi_{i,j+1} - \phi_{i,j})$$

$$X_{i,j-\frac{1}{2}} = -\frac{q\mu_{i,j-\frac{1}{2}}^k}{D_{i,j-\frac{1}{2}}^k}(\phi_{i,j} - \phi_{i,j-1})$$

The superscript  $k$  and  $k+1$  represent the previous and current time level. The transport properties such as  $D_{i+\frac{1}{2},j}^k$  are evaluated by the average values of adjacent cells, for example,

$$D_{i+\frac{1}{2},j}^k = \frac{1}{2}(D_{i+1,j}^k + D_{i,j}^k) \quad (31)$$

Similarly, the complete form of energy equation can be written as

$$\begin{aligned} \frac{\partial n_{\varepsilon(i,j)}}{\partial t} + \frac{\partial \Gamma_{\varepsilon(i,j)}}{\partial x} + \frac{\partial \Gamma_{\varepsilon(i,j)}}{\partial y} &= S_{i,j} \\ \Rightarrow \frac{n_{\varepsilon(i,j)}^{k+1} - n_{\varepsilon(i,j)}^k}{\Delta t} + \frac{\Gamma_{\varepsilon(i+\frac{1}{2},j)}^{k+1} - \Gamma_{\varepsilon(i-\frac{1}{2},j)}^{k+1}}{\Delta x_{i,j}} + \frac{\Gamma_{\varepsilon(i,j+\frac{1}{2})}^{k+1} - \Gamma_{\varepsilon(i,j-\frac{1}{2})}^{k+1}}{\Delta y_{i,j}} &= S_{\varepsilon(i,j)} \end{aligned} \quad (32)$$

where

$$\Gamma_{\varepsilon(i+\frac{1}{2},j)}^{k+1} = -\frac{5}{3} \frac{D_{i+\frac{1}{2},j}^k}{x_{i+1,j} - x_{i,j}} \left[ B(-X_{i+\frac{1}{2},j}) n_{\varepsilon(i+1,j)}^{k+1} - B(X_{i+\frac{1}{2},j}) n_{\varepsilon(i,j)}^{k+1} \right]$$

$$\Gamma_{\varepsilon(i-\frac{1}{2},j)}^{k+1} = -\frac{5}{3} \frac{D_{i-\frac{1}{2},j}^k}{x_{i,j} - x_{i-1,j}} \left[ B(-X_{i-\frac{1}{2},j}) n_{\varepsilon(i,j)}^{k+1} - B(X_{i-\frac{1}{2},j}) n_{\varepsilon(i-1,j)}^{k+1} \right]$$

$$\Gamma_{\varepsilon(i,j+\frac{1}{2})}^{k+1} = -\frac{5}{3} \frac{D_{i,j+\frac{1}{2}}^k}{y_{i,j+1} - y_{i,j}} \left[ B(-X_{i,j+\frac{1}{2}}) n_{\varepsilon(i,j+1)}^{k+1} - B(X_{i,j+\frac{1}{2}}) n_{\varepsilon(i,j)}^{k+1} \right]$$

$$\Gamma_{\varepsilon(i,j-\frac{1}{2})}^{k+1} = -\frac{5}{3} \frac{D_{i,j-\frac{1}{2}}^k}{y_{i,j} - y_{i-1,j}} \left[ B(-X_{i,j-\frac{1}{2}}) n_{\varepsilon(i,j)}^{k+1} - B(X_{i,j-\frac{1}{2}}) n_{\varepsilon(i,j-1)}^{k+1} \right]$$

Note that  $n_\varepsilon = n_e \bar{\varepsilon} = n_e \left( \frac{3}{2} k_B T_e \right)$ , where  $k_B$  is the Boltzmann constant. The source term of electron energy density equation can be represented explicitly as

$$\begin{aligned} S_{\varepsilon(i,j)}^k &= -e \bar{\Gamma} \cdot \bar{E} - \sum_{m=1}^{S_e} \varepsilon_m S_{m(i,j)}^k + 3 \frac{m}{M} n_e \nu_m \left( T_{e(i,j)}^k - T_{g(i,j)} \right) \\ &\Rightarrow -e \left( \Gamma_{x(i,j)}^k \cdot E_{x(i,j)}^k + \Gamma_{y(i,j)}^k \cdot E_{y(i,j)}^k \right) - \sum_{m=1}^{S_e} \varepsilon_m S_{m(i,j)}^k + 3 \frac{m}{M} (n_e \nu_m)^k \left( T_{e(i,j)}^k - T_{g(i,j)} \right) \end{aligned} \quad (33)$$

The complete discretized form of Poisson equation can be written as

$$\begin{aligned} \nabla \cdot (\varepsilon \nabla \phi) &= \sum_{m=1}^{\alpha} q_m n_{m(i,j)} \\ &\Rightarrow \frac{1}{\Delta x_{i,j}} \left[ \frac{\varepsilon_{i,j} \varepsilon_{i+1,j}}{\varepsilon_{i,j} \Delta h_{x(i+1,j)} + \varepsilon_{i+1,j} \Delta h_{x(i,j)}} (\phi_{i+1,j}^{k+1} - \phi_{i,j}^{k+1}) - \frac{\varepsilon_{i-1,j} \varepsilon_{i,j}}{\varepsilon_{i-1,j} \Delta h_{x(i,j)} + \varepsilon_{i,j} \Delta h_{x(i-1,j)}} (\phi_{i,j}^{k+1} - \phi_{i-1,j}^{k+1}) \right] + \\ &\frac{1}{\Delta y_{i,j}} \left[ \frac{\varepsilon_{i,j} \varepsilon_{i+1,j}}{\varepsilon_{i,j} \Delta h_{y(i+1,j)} + \varepsilon_{i+1,j} \Delta h_{y(i,j)}} (\phi_{i,j+1}^{k+1} - \phi_{i,j}^{k+1}) - \frac{\varepsilon_{i-1,j} \varepsilon_{i,j}}{\varepsilon_{i-1,j} \Delta h_{y(i,j)} + \varepsilon_{i,j} \Delta h_{y(i-1,j)}} (\phi_{i,j}^{k+1} - \phi_{i,j-1}^{k+1}) \right] \\ &= \sum_{m=1}^{\alpha} q_m n_{m(i,j)}^k \end{aligned} \quad (34)$$

## 2.4 Numerical Algorithm

The governing equations of plasma fluid modeling are solved implicitly with backward Euler method in time and independently as shown in Figure 2. 2. The program starts from the evaluation of transport properties, source of each species continuity equation, and source of electron energy density equation. At each time step, the resulting algebraic linear system of each equation is solved independently by the GMRES with or without parallel ASM preconditioner provided by PETSc library [Balay *et al.*, 2001] through domain decomposition technique on the top of MPI protocol. Among the iterative linear solvers of Krylov subspace, we select the GMRES to solve the linear systems obtained by discretization since it has been shown to be the most robust linear matrix solver for most of the cases. In addition, in the preconditioning we test the performance of two sub-domain solvers such as LU (direct) and incomplete LU (ILU; iterative) factorizations. Other preconditioners

using, for example, Jacobi and successive over relaxation (SOR) do not converge well in the current study and are generally very time-consuming, and are thus excluded for further discussion.

## 2.5 Experimental Methods

Figure 2. 3 illustrates the schematic diagram of a parallel-plate DBD atmospheric-pressure plasma jet (APPJ) along with gas supply system and the instrumentation for voltage and current measurements. This APPJ consists of two parallel copper electrodes ( $50 \times 50 \times 8$  mm each) with embedded cooling water. Each electrode is covered with a ceramic plate in the size of  $70 \times 70 \times 2$  mm for inactivation/sterilization application and a quartz plate in the size of  $70 \times 70 \times 1$  mm for surface hydrophilic modification application. The dielectric plates are 5 mm extruded from the end of the electrodes (in the flow direction), which can prevent the electrode assembly from arcing. Distance between the two dielectric plates (ceramic/quartz) was kept as 1 mm throughout the study. The assembly of electrodes and dielectrics were then covered by an insulation layer made of Teflon to provide safety and prevent arcing problem during operation.

This DBD assembly was powered by a distorted sinusoidal voltage (quasi-pulsed) power supply (Model Genius-2, EN Technologies Inc.). This power supply facilitates adjustment of frequency (20~60 KHz), power density (low/middle/large), peak current (max. 4A), peak voltage (max. 15 kV), and power (max. 2 kW). Resulting output voltage waveform of the power supply produces the voltage increase, which can possibly enhance the plasma properties. The distorted sinusoidal voltage power feature is generated high voltage with high  $dv/dt$  to enhance radical generation.

Input voltage and output current waveform across the electrodes of the

parallel-plate discharge were measured by a high-voltage probe (Tektronix P6015A) and a current monitor (IPC CM-100-MG, Ion Physics Corporation Inc.), respectively, through a digital oscilloscope (Tektronix TDS1012B). The current monitor belong Rogowski coil type. The output sensitivity is 1 volts/Amp, and hole diameter is 0.5 inch to suit insulating power cable. The Rogowski coil used for fast current changing measurement better than the Hall effect device.

## 2.6 Kinetic Model

The 0D kinetic model will be detailed, describing the evolution of  $N_2$  and  $N_2 + O_2$  neutral particles. The data on the processes of excitation and ionization in nitrogen based are reviewed in [Gadd *et al.*, 1990; Kossyi *et al.*, 1992; Capitelli *et al.*, 2000; Balay *et al.*, 2001; Golubovskii *et al.*, 2002; Pintassilgo *et al.*, 2005; Choi *et al.*, 2006; Panousis *et al.*, 2009; Tochikubo *et al.*, 2009; Tsai *et al.*, 2010]. The discharge in nitrogen and oxygen is characterized by a wide variety of elementary processes. This is a common feature of molecular gases.

For the pure nitrogen reaction channels are summarized in [Table 2](#):. The  $N_2$  plasma chemistry employed in the present study includes 11 species (electron, N,  $N(^2D)$ ,  $N_2$ ,  $N_2^+$ ,  $N_4^+$ ,  $N_2(X^1\Sigma_g^+, \nu = 1-6)$ ,  $N_2(A^3\Sigma_u^+)$ ,  $N_2(B^3\Pi_g)$ ,  $N_2(C^3\Pi_u)$ ,  $N_2(a^1\Sigma_u^-)$ ) and 34 reactions. Note we have ignored the  $N^+$  and  $N_3^+$  in the simulation since they have been found to unimportant in nitrogen plasma simulation [Golubovskii *et al.*, 2002]. Furthermore, the number density of background nitrogen does not change with time or position is assumed.

First, the vibrational excitation of a molecule in the ground state must be taken into account for a proper description of the kinetics of excitation. As the density of vibrationally excited molecules is high enough, the electron distribution function is

deformed due to superelastic collisions and the rate of direct excitation and ionization increases. The influence of the vibrational excitation over the electron distribution function was studied in [Loureiro et al. 1986]. Therefore, we have chosen to take into account of the levels up to  $v = 6$  using cross sections data from BOLSIG+ [Balay *et al.*, 2001] for the electronic excitation of the vibrational levels of the ground state in this work (Reactions 3-10 in [Table 2](#)). Second, since the number of excited states for the nitrogen molecule is rather high, especially an important excited species of the lowest metastable state  $N_2(A^3\Sigma_u^+)$ . This state usually has the largest lifetime (more than 1 second) in comparison with higher excited states. Therefore, the triplet states  $N_2(A^3\Sigma_u^+)$ ,  $N_2(B^3\Pi_g)$ ,  $N_2(C^3\Pi_u)$  and singlet state  $N_2(a^1\Sigma_u^-)$  of molecular nitrogen are considered. Reactions 11-14 describe the electronic excitation of the ground state nitrogen molecule to the vibrational levels of the  $N_2(A^3\Sigma_u^+)$ ,  $N_2(B^3\Pi_g)$ ,  $N_2(C^3\Pi_u)$ ,  $N_2(a^1\Sigma_u^-)$  excited states which the cross sections data take from BOLSIG+ [Balay *et al.*, 2001]. In addition, reactions 31-34 represent the radiative decay of those excited states. Third, Pointu [Pointu *et al.*, 2005] and Panousis [Panousis *et al.*, 2009] experimentally estimated the N-atom was the most dominant atom species with a density of  $\sim 10^{15} \text{ cm}^{-3}$ . Hence the ground state of N-atom reacted channels had considered in Reactions 15-17. Fourth, according to the literature [Panousis *et al.*, 2007], the dominant ionic species in atmospheric pressure conditions are considered to be  $N_4^+$ , due to the very efficient conversion mechanism in Reactions 19 that imposes on  $N_2^+$  ions an effective lifetime below 1 ns. Fifth, collisions between two nitrogen metastable molecules create seed electrons via ionization by Penning effect as shown in Reactions 21 and 22. Sixth, the gas temperature, necessary for the calculation of the coefficients of Reactions 16 and 18,

was taken equal to  $T_g = 400$  K, close to an experimental estimation [Panousis *et al.*, 2007].

For the  $N_2 + O_2$  reaction channels are summarized in [Table 3](#). The total number of reactions between various particles in  $N_2/O_2$  discharges exceeds 450 [Kossyi *et al.*, 1992]. But the atmospheric BD has two features, which makes it possible to simplify the common model of the excitation kinetics. First, the ionization degree is rather small, since the experimentally observed discharge mode is a Townsend-like discharge or local microdischarge. Second, the admixture of oxygen does not exceed 0.1 % of the total gas volume. A small amount of oxygen allows us to exclude the reactions nonlinear in  $O_2$  density. In this study, the  $N_2/O_2$  plasma chemistry employed in the present study includes 24 species (electron, N,  $N(^2D)$ ,  $N_2$ ,  $N_2^+$ ,  $N_4^+$ ,  $N_2(X^1\Sigma_g^+, \nu=1-6)$ ,  $N_2(A^3\Sigma_u^+)$ ,  $N_2(B^3\Pi_g)$ ,  $N_2(C^3\Pi_u)$ ,  $N_2(a^1\Sigma_u^-)$ ,  $O_2$ ,  $O_2^+$ ,  $O_2^-$ ,  $O^-$ ,  $O_2(a)$ , O,  $O(^1D)$ ,  $O(^1S)$ ,  $O_3$ , NO, NO(A), NO(B),  $O(^1S)N_2$ ) and 85 reactions. The added oxygen gas operates as a quencher of electron and metastable molecules, resulting in the density decreases of metastable species as well as electrons. Therefore, the small content oxygen can significantly affect the plasma sustain.

## **Chapter 3 One-Dimensional Simulation of Nitrogen Dielectric Barrier Discharge Driven by a Quasi-pulsed Power Source and Its Comparison with Experiments**

A frame work of pure nitrogen results and discussions are revealed in [Figure 3. 1](#). Three distinct parts for nitrogen DBD results are introduced: verification of the simulated results with experimental measurements, basic discharge structure and parameter studied.

### **3.1 Verification of the Fluid Modeling and Kinetic Model**

To validate the fluid modeling code in nitrogen kinetic model, we have simulated an one-dimensional cases and results were compared with previous experimental data. The experiment is produced between two plane electrodes, 3.2 cm in diameter and covered by a dielectric barrier made of a 635  $\mu\text{m}$  alumina plate (the permittivity was set 9.0 in this simulation).The interdielectric gap is fixed at 1 mm. Its frequency is set sinusoidal form AC 8 kHz, and its amplitude is chosen 6 kV in atmospheric pressure. [Figure 3. 3](#) shows the comparison of the simulated discharged currents (upper) with the experimental measured data (bottom) from [Gherardi *et al.*, 2001]. It clearly shows that the present fluid modeling code using the nitrogen plasma chemistry can predict quantitatively the temporal evolution of discharge current of experimental measured discharge very well.

### **3.2 Simulation Conditions**

The atmospheric-pressure parallel-plate DBD consists of two electrodes (5x5



cm), each covered by an alumina dielectric (95% Al<sub>2</sub>O<sub>3</sub> with  $\epsilon=12.63$ ) with 2 mm in thickness. The distance between the two dielectric layers is 0.5 mm throughout the study. A distorted sinusoidal voltage waveform having peak value of 6.6 kV with a frequency of 60 kHz was used to sustain the discharge throughout the study unless otherwise specified. Related experimental setup had been described in detail in [Chiang *et al.*, 2010] and is not repeated here for brevity. Because the input voltage was not a sinusoidal waveform, it was fitted by a Fourier series with 18 terms using 60 kHz as the fundamental frequency in the simulation. The mesh criterion used 200 cells/mm, because the results in [Table 4](#) are almost constant when the mesh numbers are more than 200 cells/mm. Generally, 3-5 cycles of simulation are enough for reaching a quasi-steady state solution. Only the data at 4<sup>th</sup> cycle are presented for the purpose of discussion.

### 3.3 Basic Discharge Structure

[Figure 3. 3](#) shows that comparison of simulated and measured discharged currents of nitrogen DBD along with the experimental photo image (0.2 s exposure time) of discharge at the bottom. Homogeneous light emission justifies the use of 1-D fluid modeling for this problem. Note the various currents in the simulation are defined as follows:

$$J_{total}(t, x) = J_{displacement}(t, x) + J_{conduction}(t, x)$$

$$J_{displacement}(t, x) = \epsilon \frac{\partial E}{\partial t}$$

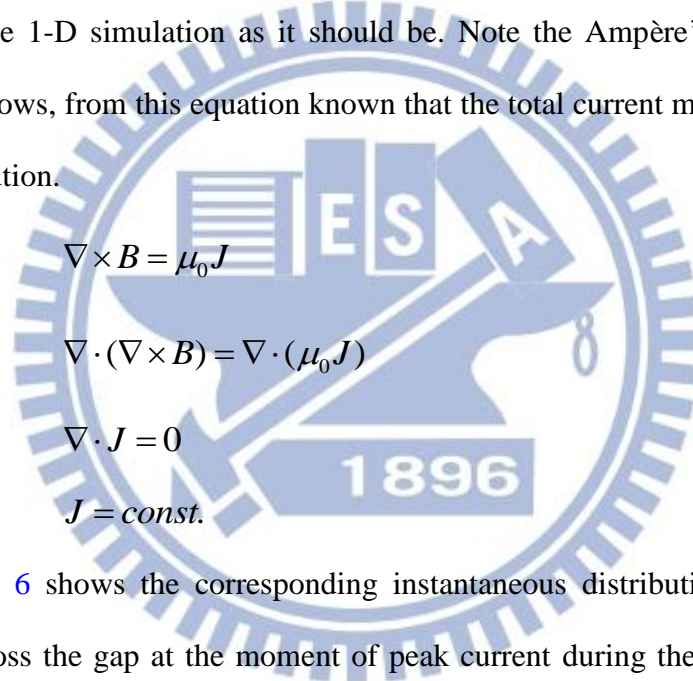
$$J_{conduction}(t, x) = \pm \sum e \Gamma_{e, N_2^+, N_4^+}$$

Results show that simulated discharge currents are in good quantitative agreement with the experimental data throughout the cycle. The discharge current has the form of two major peaks per cycle and each peak has a duration of approximate 2  $\mu$ s, in

which the current intensity is about 10~20 mA/cm<sup>2</sup>. In addition, the current peaks are much wider as compared to narrow peaks in helium discharges under similar conditions [Massines et al., 1998].

Figure 3. 4 shows the various spatial averaged current densities during a cycle. During the breakdown, the conduction currents are much higher than the displacement current, in which N<sub>4</sub><sup>+</sup> is dominant. In the post-breakdown period, the displacement current is dominant, and the discharge almost extinguishes.

Figure 3. 5 shows the current continuity across the gap during the breakdown is enforced in the 1-D simulation as it should be. Note the Ampère's circuital law is defined as follows, from this equation known that the total current must be constant in spatial distribution.



$$\begin{aligned}\nabla \times B &= \mu_0 J \\ \nabla \cdot (\nabla \times B) &= \nabla \cdot (\mu_0 J) \\ \nabla \cdot J &= 0 \\ J &= \text{const.}\end{aligned}$$

Figure 3. 6 shows the corresponding instantaneous distributions of discharge properties across the gap at the moment of peak current during the breakdown. It is observed that the electric field is almost linear (from 55 to 60 kV/cm) across the gap because of the low net charge density (difference between positive ions and electron), which is unlike a typical glow discharge with a quasi-neutral region. Number density of N<sub>4</sub><sup>+</sup> is much higher than that of electron across the gap. In addition, electron number density decreases exponentially with increasing distance from the powered electrode (anode at the left side). These results are similar to some earlier studies in atmospheric-pressure nitrogen discharges [Golubovskii et al., 2002; Choi et al., 2006; Massines et al., 2009]. Interestingly, the density of N<sub>2</sub><sup>+</sup> species produced by electron

direct ionized was two orders of magnitude lower than that of  $N_4^+$  during the breakdown. It was noted that, the conversion mechanism of the  $N_2^+$  ion into the  $N_4^+$  ion (Reaction 20 in [Table 2](#)) was very efficient [Golubovskii *et al.*, 2002; Panousis *et al.*, 2007]. It is also found that the electron energy density ( $\varepsilon_e = \frac{3}{2}n_e kT_e$ ) peaks near the powered electrode because more electrons are attracted and generated. In addition, the electron temperature is close to 5 eV throughout the gap.

[Figure 3. 7](#) shows instantaneous distributions of discharge properties across the gap at the moment of negligible current after the breakdown.  $N_4^+$  ( $\sim 10^{14} \text{ m}^{-3}$ ) is also found to be most dominant charged species at this moment, but the amount of density is less than two orders during the breakdown period as presented in [Figure 3. 6](#). This is caused by the continuing associate ionization between the remaining long-lived metastable nitrogen species (Reactions 21 and 22 in [Table 2](#)). In addition, number densities of  $N_2^+$  and electron become as low  $\sim 10^8$  and  $\sim 10^{11} \text{ m}^{-3}$ , respectively, because there is no direct ionization at this moment. It is mainly because the electron energy density becomes much lower,  $\sim$  four orders of magnitude lower with electron temperature of  $\sim 2$  eV, as compared to that in the breakdown period which leads to no direct ionization in this post-breakdown period.

### 3.4 Effect of Gap Distance

[Figure 3. 8](#) shows that comparison of simulated discharged currents of nitrogen DBD driven by a quasi-pulsed power (60 kHz) for different gap distances (0.5, 0.7, 1.0 and 1.4 mm) along with the experimental photo images of discharge on the right. Note the measured relative permittivity and thickness of the ceramic material is 12.63 and 2 mm in 60 kHz frequency and 6800 V applied voltage distorted sinusoidal wave form.

In Figure 3. 8 (a) (b), the simulated currents are agreed well with experimentally measured currents. For the cases of smaller gap (0.5, and 0.7 mm), the simulations demonstrate they are typically homogeneous Townsend-like discharges with much fewer electrons than ions (not shown here). In addition, the experimental photo images showed that the plasma regions are uniform. For the case of larger gap (d=1.0 mm), the simulation shows it is a glow-like discharge with very high current density during the breakdown phase. This is attributed to the fact that the discharge has transitioned from Townsend-like to filamentary-like (microdischarge). However, this is obviously against the measurements in larger gap non-uniform case as shown in the photo images in Figure 3. 8 (c). This shows that one has to be very cautious about the use of one-dimensional fluid modeling for simulating the non-uniform parallel-plate nitrogen DBD. 1-D fluid modeling can get good result in uniform case include Townsend (0.5, 0.7 mm) and no breakdown (1.4 mm), but dismiss in unstable and non-uniform filamentary case (1.0 mm), which makes the one-dimensional fluid modeling invalid.

### 3.5 Effect of External Driving Voltage

Figure 3. 9 presents the cycle-space averaged number densities of various species with peak voltages in the range of 6.2-8.6 kV with a gap distance of 0.5 mm and two ceramic layers of 2.0 mm in thickness. Generally, number densities of all species increase exponentially with the magnitude of applied peak voltage. The ion density ( $\sim 10^{16} \text{ m}^{-3}$ ) is three orders of magnitude higher than the electron density ( $\sim 10^{13} \text{ m}^{-3}$ ). The metastable species  $N_2(A^3\Sigma_u^+)$  and atom nitrogen are the most dominant species with a number density of  $10^{19} \sim 10^{21} \text{ m}^{-3}$ , which agrees reasonably well with the experimental measurements [Dilecce *et al.*, 2007; Panousis *et al.*, 2009]. It should be

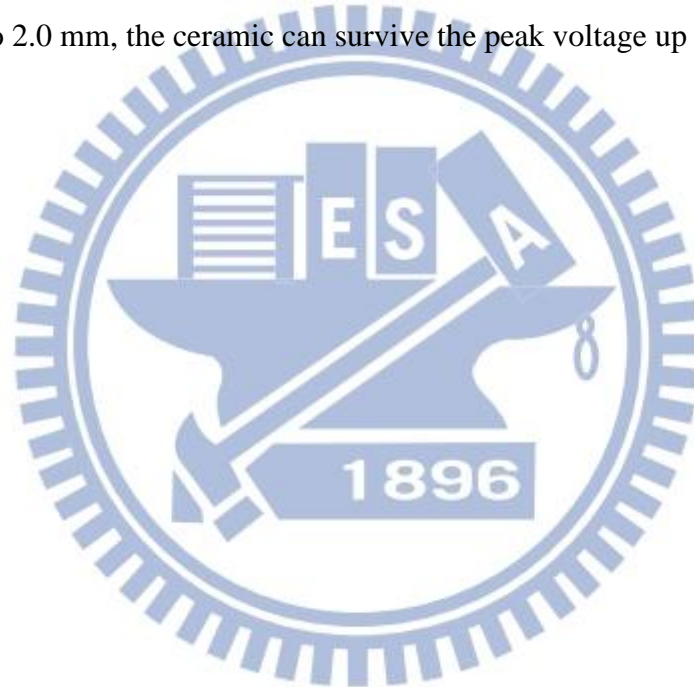
noted that the number densities of all species increase with increasing applied voltage; however, the dielectric material may become more vulnerable with increasing applied voltage. [Table 5](#) summarizes the average absorbed powers of electron and ions at different applied peak voltages. The electron absorbed power is generally less than one order of the  $N_4^+$  absorbed power. This is unlike most glow-like discharges driven by radio-frequency (RF) power sources, in which most electric power is absorbed by the electrons instead. However, gas heating often increases with increasing ion absorbed power due to the efficient energy transfer between ions and background neutrals [Jou *et al.*, 2010].

### 3.6 Effect of Dielectric Material

[Figure 3. 10](#) and [Figure 3. 11](#) show the discharge current, gap voltage and accumulated charges on both dielectric surfaces for materials of ceramic ( $\epsilon = 12.63$ ) and quartz ( $\epsilon = 4.76$ ) with 2.0 mm in thickness respectively. The gap distance between dielectric is kept the same as 0.5 mm. The applied peak voltage is 8,600 V which can sustain the nitrogen DBD with two quartz dielectrics using a power source with a frequency of 60 kHz. Results show that the larger permittivity of the dielectric material is the larger the discharge current and the longer the period is. In addition, the quantity of accumulated charge at each electrode increases with increasing permittivity of the dielectric material. This is especially important that negative accumulated charges at the dielectric surface provide the mechanism of preventing arc occurrence in nitrogen DBD by decreasing the gap voltage at the powered side. These results coincide with those observed previously in [Golubovskii *et al.*, 2006], in which also showed that larger applied voltage is required to sustain the discharge when the permittivity is smaller.

### 3.7 Effect of Dielectric Thickness

*Table 6* summarizes the average number densities and absorbed power at two different thicknesses of ceramic layer (1.0 and 2.0 mm). Simulation conditions include gap distance of 0.5 mm, applied peak voltage of 6,200 V and a frequency of 60 kHz. Results show that average number densities and plasma absorbed power decrease dramatically with increasing thickness. It is noted that the discharge with a ceramic layer of 1 mm in thickness is much easier to sustain in the experiments, but the operating voltage peak is limited up to 6.4 kV without damage. As the thickness increases up to 2.0 mm, the ceramic can survive the peak voltage up to 9.0 kV.



## **Chapter 4 Numerical Investigation of Effects of Oxygen Addition on a Nitrogen-based Dielectric Barrier Discharge and Its Comparison with Experiments**

A frame work of oxygen addition on nitrogen-based results and discussions are revealed in [Figure 4. 1](#). Three distinct parts for  $N_2 + O_2$  DBD results are introduced: basic discharge structure, the effects of trace oxygen on nitrogen-based DBD and verification of the simulated results with experimental measurements.

### **4.1 Simulation Conditions**

The parallel-plate (5x5 cm), atmospheric DBD consists of two electrodes, both covered by a quartz dielectric (measured  $\epsilon = 4.76$ ), having 1 mm in thickness each. The gap between the quartz plates is 1 mm throughout the study. A distorted sinusoidal waveform with a frequency of 60 kHz and 8200 V applied voltage was used to sustain the discharge. The Fourier series with 18 terms using 60 kHz as the fundamental frequency was employed to fit the measured voltage as simulated input voltage. 400 non-uniform grid points and  $2 \times 10^{-12}$  seconds of time step are used for simulations throughout the study unless otherwise specified. Only the data at 4<sup>th</sup> cycle are presented for the purpose of discussion.

### **4.2 Basic Discharge Structure**

[Figure 4. 2](#) shows that comparison of simulated and measured discharged currents for  $N_2$  with 0.03 %  $O_2$  admixture. Results show that simulated discharge currents are in good quantitative agreement with the experimental data. Due to the

applied voltage was distorted sinusoidal waveform. The discharge current has the form of two major peaks per half cycle and each peak has duration of approximate 2  $\mu$ s. The first peak was formed during 0-2  $\mu$ s and had the maximum current density about 20 mA/cm<sup>2</sup>. In addition, the region between 2-4  $\mu$ s had strong voltage variation with time. Therefore the second peak was formed and the current density was about 10 mA/cm<sup>2</sup>. In [Maiorov *et al.*, 2007] experimental and numerical studies show that as the oxygen content increased, the multiple peaks current was appeared. Furthermore, as the amount of oxygen more than 1000 ppm, the discharge transferred in filamentary mode. The current of Figure 4. 2 was not revealed the multiple peaks phenomenon; therefore the one-dimensional simulation was still suited in this study.

Figure 4. 3 and Figure 4. 4 shows the N<sub>2</sub> + 0.03% O<sub>2</sub> spatial-average temporal discharge properties with a 60 kHz cycle. In the charges density Figure 4. 3 found that the dominate species are N<sub>4</sub><sup>+</sup> and O<sub>2</sub><sup>-</sup> with about 10<sup>18</sup> m<sup>-3</sup> density, both species showed quasi-neutral with all temporal variations. In addition, it is interesting in electron density variations with time in DBD plasma. The electron density was between 10<sup>14</sup>-10<sup>15</sup> m<sup>-3</sup> as the plasma extinguished and was less than 10<sup>16</sup> m<sup>-3</sup> as the plasma ignited. It is weakly discharge comparing with typical atmospheric pressure glow discharge (10<sup>16</sup>-10<sup>17</sup> m<sup>-3</sup>) [Massines *et al.*, 2007]. Because the small amount seeds of electron, the generations of plasma more depended on electron energy. Figure 4. 3 showed that the applied voltage had an abrupt variation between 0-4  $\mu$ s and to follow a smooth change between 4-8.3  $\mu$ s. The rapid voltage variations made the electron to obtain enough energy (more than 2 eV) to ignite the plasma, therefore the ionized species of N<sub>2</sub><sup>+</sup> and O<sub>2</sub><sup>+</sup> greatly increased. The Figure 4. 4 showed the neutral species densities variations with time. The species of N<sub>2</sub>(A<sup>3</sup> $\Sigma_u^+$ ), N<sub>2</sub>(B<sup>3</sup> $\Pi_g$ ), N<sub>2</sub>(C<sup>3</sup> $\Pi_u$ ), N<sub>2</sub>(a<sup>1</sup> $\Sigma_u^-$ ) were generated by electron direct excited (Reactions 11-14 in Table 3) and



they apparent depended on electron energy, too. Due to the metastable  $N_2(A^3\Sigma_u^+)$  has more than 1s lifetime, the density profile almost was not change with time. In the other hand, the densities of  $N_2(A^3\Sigma_u^+)$  and atom nitrogen were about  $4 \times 10^{19} \text{ m}^{-3}$  and  $1 \times 10^{21} \text{ m}^{-3}$ . Those results are agreed with experimentally estimated in [Panousis *et al.*, 2009]. This reference also showed that the impurity oxygen has greatly efficiently even in few ppm level, furthermore estimated the atom oxygen had the order of  $10^{17} \text{ m}^{-3}$ . The atom density is about  $6 \times 10^{20} \text{ m}^{-3}$  in this study, it may be the addition of oxygen is hundred ppm level.

#### 4.4 Influence of Trace Oxygen on Cycle Average Properties

The cycle average of different species density for trace oxygen (0.003% to 0.1%) shows in Figure 4. 5. First, the electron density greatly decreased from the order  $10^{17} \text{ m}^{-3}$  to  $10^{14} \text{ m}^{-3}$  as the trace oxygen increased. Therefore, the small content oxygen can significantly affect the plasma sustain. Second, the excited state density of nitrogen species  $N_2(A^3\Sigma_u^+)$ ,  $N_2(B^3\Pi_g)$ ,  $N_2(C^3\Pi_u)$ ,  $N_2(a^1\Sigma_u^-)$  appeared a rapid increase before the oxygen content reached 100 ppm, and followed a slow decrease. Those species came from by directly electron excited, as the trace oxygen below 0.01 % the electron density still had more than  $10^{16} \text{ m}^{-3}$ . In the other hand, the electron energy increased from 0.93 eV to 1.8 eV. Therefore, as the electron density retained enough quantity, the raise electron energy increased the excited species densities. Although the electron energy keep increased to 2.9 eV as the additions of oxygen arrived 0.1 %, but the electron density was enormous decreased to  $10^{14} \text{ m}^{-3}$ . Therefore those excited species densities decreased with oxygen content after 100 ppm. Third, the ground state of atom oxygen and nitrogen revealed a slight changed with the trace oxygen added. Both species not only depended on electron disassociated, but also came from

complex neutral species interacted. Hence, the densities of atom oxygen and nitrogen just varied between  $4.0 \times 10^{20} \text{ m}^{-3}$  to  $5.7 \times 10^{20} \text{ m}^{-3}$  and  $1.0 \times 10^{21} \text{ m}^{-3}$  to  $1.2 \times 10^{21} \text{ m}^{-3}$ . Fourth, the species of  $\text{O}_3$  and  $\text{NO}$  were not produced by electron collided directly. As the trace oxygen gradually raised, both species densities increased from 0.003% to 0.1% oxygen content. This trace showed that the  $\text{O}_3$  and  $\text{NO}$  species more depended on trace oxygen density. Besides, the small additions of oxygen can produce more than  $10^{19} \text{ m}^{-3}$  density of ozone and  $\text{NO}$ . Therefore the  $\text{N}_2/\text{O}_2$  DBD plasma has good potential for many industry applications.

#### 4.5 Influence of Trace Oxygen on Spectroscopic Properties

The calculated radiations in this study (full curves) and experimental optical emission spectrums in [Brandenburg *et al.*, 2005] (dashed curves) were compared as a function of the trace oxygen in Figure 4. 6. The spectral bands of second positive system of  $\text{N}_2$  (Reaction 80 in Table 3),  $\text{NO}\gamma$ -system (Reaction 83 in Table 3) and  $\text{ON}_2$ -excimer (Reaction 85 in Table 3) were selected. The theory and experiment results had a similar trace: a rapid rise followed a slow decay. The differences of the maximum intensity between simulations and measurements may be due to the impurities from feeding gas (10-20ppm) [Brandenburg *et al.*, 2005]. The SPS spectrum was depended on  $\text{N}_2(\text{C}^3\Pi_u)$  species; therefore the trend was the same as the excited state of nitrogen species in section 3.2. The spectrums of  $\text{NO}\gamma$  and  $\text{ON}_2$ -excimer increased with the oxygen added below 100 ppm. The phenomenon was due to the increased of oxygen species. The  $\text{N}_2(\text{A}^3\Sigma_u^+)$  is an important source to excite the  $\text{NO}$  and  $\text{O}$ , but the  $\text{N}_2(\text{A}^3\Sigma_u^+)$  was quenched efficiently by molecular oxygen [Brandenburg *et al.*, 2005]. Therefore, both spectrums decreased as the oxygen contents continued increased.

## **Chapter 5 Conclusion and Recommendations of Future Work**

### **5.1 Summary Remarks**

In the present study, we have investigated in detail the non-equilibrium atmospheric-pressure dielectric barrier discharge driven by a realistic distorted-sinusoidal voltage power source (60 kHz) using a self-consistent one-dimensional fluid modeling code considering non-local electron energy transport. The experiment data are compared with the calculations results. A benchmark case (with 60 kHz, 6800 V, 0.5mm gap, 2.0 mm ceramic dielectric thickness, 1 atm) shown that simulation results are quantitatively agree with experiment.

The fluid modeling simulation of dielectric barrier discharge (DBD) with pure nitrogen gas is presented. All the model equations, species continuity equations, electron energy equation and Poisson's equation, are non-dimensionalized and discretized by fully-implicit backward Euler finite-difference method with Scharfetter-Gummel scheme for calculating the flux of charged species. The nonlinear coupled equations are solved by Newton-Krylov-Swartz (NKS) algorithm with additive Schwarz (AS) preconditioner.

### **5.2 Summary of Pure Nitrogen DBD Plasma**

1. In the framework of the model, the influence of gap distance between dielectric had been investigated. It was shown in the same applied voltage, the breakdown time delay and plasma sustain time decrease when gap distance increase. Experimental photo images show mode transition while gap distance varies from 0.7 to 1 mm. Therefore, 1D code cannot represent the experiment results while gap distance is larger than 1mm, because of the non-uniform discharge between

the electrodes. This shows that one has to be very cautious about the use of one-dimensional fluid modeling for simulating the non-uniform parallel-plate nitrogen DBD.

2. The discharge properties are studied by varying the applied voltage of external power source. Higher plasma density can be obtained by increase with the external applied voltage. Although the higher voltage was easier to sustain plasma, but the higher voltage was easier damage the dielectric material also. In energy absorbed, the  $N_2^+$  ion gain the most power than electron about one order in our simulation case.
3. The effects of the dielectric properties are proposed. As the gas voltage polarity changes, the larger dielectric constant has more accumulated electron seed to ionize and to sustain the plasma. Therefore, the plasma density and current increased with dielectric constant.
4. In the other hand, the dielectric thickness great influenced the plasma density and power absorbed in plasma. The thinner dielectric was easier sustained the plasma and got higher plasma density. But the operated amplitude was limited in smaller range because the too high energy will break the dielectric.

### 5.3 Summary of $N_2/O_2$ DBD Plasma

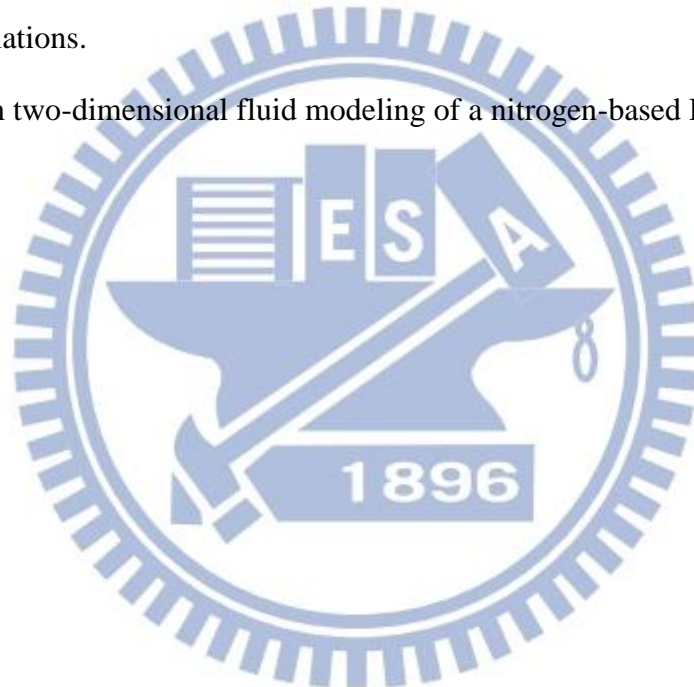
1. Since the real working gas is not absolutely clean, an interesting parameter in the nitrogen discharge is the density of the admixture. When the nitrogen contains some promille of oxygen, the discharge tends to be filamentary in the same geometry, voltage and frequency.
2. When the trace oxygen increased, the total current relatively decreased. The electron attached to  $O_2^-$  apparent increases. Generated electrons are attached with oxygen which decreases the electron density. The electron density linear

decreased as the trace oxygen increased. Therefore, the small content oxygen can significantly affect the plasma sustain.

## 5.4 Recommendations of Future Work

According to this study, the planned future, tasks are summarized as follows:

1. To study the effect of operating parameters of  $N_2/O_2$  plasma including applied power frequency, voltage waveform, dielectric property, dielectric thickness...
2. To compare with measured OES light emission data for the species calculated from simulations.
3. To perform two-dimensional fluid modeling of a nitrogen-based DBD.



## References

- [1] Brandenburg, R., Maiorov, V. A., Golubovskii, Y. B., Wagner, H. E., Behnke, J. and Behnke, J. F., "Diffuse barrier discharges in nitrogen with small admixtures of oxygen: discharge mechanism and transition to the filamentary regime", *Journal of Physics D: Applied Physics* 38: (2005) 2187.
- [2] Bukowski, J. D., Graves, D. B. and Vitello, P., "Two-dimensional fluid model of an inductively coupled plasma with comparison to experimental spatial profiles", *Journal of Applied Physics* 80: (1996) 2614.
- [3] Balay, S., Gropp, W. D., McInnes, L. C. and Smith, B. F., "Petsc home page", 2001, <http://www.mcs.anl.gov/petsc/petsc-as>.
- [4] Capitelli, M., Ferreira, C. M., Gordiets B. F., and Osipov, A. I., "Plasma Kinetics in Atmospheric Gases," Springer, 2000.
- [5] Choi, Y. H., Kim, J. H. and Hwang, Y. S., "One-dimensional discharge simulation of nitrogen DBD atmospheric pressure plasma", *Thin Solid Films* 506: (2006) 389.
- [6] Dilecce, G., Ambrico, P. F. and S. D., Benedictis, "N<sub>2</sub>(A<sup>3</sup>Σ<sub>u</sub><sup>+</sup>) density measurement in a dielectric barrier discharge in N<sub>2</sub> and N<sub>2</sub> with small O<sub>2</sub> admixtures", *Plasma Sources Science and Technology* 16: (2007) 511.
- [7] Gadd, G. E., Sianger, T. G., "NO(B<sup>2</sup>Π) radiative lifetimes: v = 0-6", *Journal of Chemical Physics* 92: (1990) 2194.
- [8] Gherardi, N. and Massines, F., "Mechanisms Controlling the Transition from Glow Silent Discharge to Streamer Discharge in Nitrogen", *IEEE Transactions on Plasma Science* 29 (2001) 536.
- [9] Golubovskii, Y. B., Maiorov, V. A., Li, P. and Lindmayer, M., "Effect of the barrier material in a Townsend barrier discharge in nitrogen at atmospheric pressure", *Journal of Physics D: Applied Physics* 39: (2006) 1574.

- [10] Gogolides, Evangelos, Sawin and Herbert, H., "Continuum modeling of radio-frequency glow discharges. I. Theory and results for electropositive and electronegative gases", *Journal of Applied Physics* 72: (1992) 3971.
- [11] Grubert, G. K., Becker, M. M. and Loffhagen, D., "Why the local-mean-energy approximation should be used in hydrodynamic plasma descriptions instead of the local-field approximation", *Physical Review E* 80: (2009) 036,405.
- [12] Golubovskii, Y. B., Maiorov, V. A., Behnke, J. and Behnke, J. F., "Influence of interaction between charged particles and dielectric surface over a homogeneous barrier discharge in nitrogen", *Journal of Physics D: Applied Physics* 35: (2002) 751.
- [13] Hagelaar, G. J. M. and Kroesen, G. M. W., "Speeding Up Fluid Models for Gas Discharges by Implicit Treatment of the Electron Energy Source Term", *Journal of Computational Physics* 159: (2000) 1.
- [14] Jou, S. Y., Hung, C. T., Chiu, Y. M., Wu, J. S. and Wei, B. Y., "Simulation of Excimer Ultraviolet (EUV) Emission from a Coaxial Xenon Excimer Ultraviolet Lamp Driven by Distorted Bipolar Square Voltages", *Plasma Chemistry and Plasma Processing* 30: (2010) 907.
- [15] Kogelschatz, U., "Dielectric-barrier Discharges: Their History, Discharge Physics, and Industrial Applications", *Plasma Chemistry and Plasma Processing* 23: (2003) No. 1.
- [16] Kozlov, K. V., Brandenburg, R., Wagner, H. E., Morozov, A. M. and Michel, P., "Investigation of the filamentary and diffuse mode of barrier discharges in  $N_2/O_2$  mixtures at atmospheric pressure by cross-correlation spectroscopy", *Journal of Physics D: Applied Physics* 38: (2005) 518.
- [17] Kossyi, I. A., Kostinsky, A. Y., Matveyev, A. A. and Silakov, V. P., "Kinetic scheme of the non-equilibrium discharge in nitrogen-oxygen mixtures", *Plasma Sources Science and Technology* 1: (1992) 207.
- [18] Loureiro, J. and Ferreira, C. M., "Coupled electron energy and vibrational

- distribution functions in stationary  $N_2$  discharges”, *Journal of Physics D: Applied Physics* 19: (1986) 17.
- [19] Lymberopoulos, D. P. and Economou, D. J., “Two-dimensional simulation of polysilicon etching with chlorine in a high density plasma reactor”, *IEEE Transactions on Plasma Science* 23: (1995) 573.
- [20] Massines, F., Rabehi, A., Decomps, P., Gadri, R. B., Ségur, P. and Mayoux, “Experimental and theoretical study of a glow discharge at atmospheric pressure controlled by dielectric barrier”, *Journal of Applied Physics* 83: (1998) 2950.
- [21] Massines, F., Gherardi, N., Naudé, N. and Ségur, P., “Recent advances in the understanding of homogeneous dielectric barrier discharges”, *European Physical Journal Applied Physics*, 47: (2009) 22805.
- [22] Mangolini, L., Orlov, K., Kortshagen, U., Heberlein, J. and Kogelschatz, U., “Radial structure of a low-frequency atmospheric-pressure glow discharge in helium”, *Applied Physics Letters* 80: (2002) 1722.
- [23] Maiorov, V. A. and Golubovskii, Y. B., “Modelling of atmospheric pressure dielectric barrier discharges with emphasis on stability issues”, *Plasma Sources Science and Technology* 16: (2007) S67.
- [24] Meyyappan, M., “Computational Modeling in Semiconductor Processing”, Artech House Publishers, 1994.
- [25] Panousis, E., Ricard, A., Loiseau, J. F., Clément F. and Held, B., “Estimation of densities of active species in an atmospheric pressure  $N_2$  DBD flowing afterglow using optical emission spectroscopy and analytical calculations”, *Journal of Physics D: Applied Physics* 42: (2009) 205201.
- [26] Papageorghiou, L., Panousis, E., Loiseau, J. F., Spyrou, N. and Held, B., “Two-dimensional modelling of a nitrogen dielectric barrier discharge (DBD) at atmospheric pressure: filament dynamics with the dielectric barrier on the cathode”, *Journal of Physics D: Applied Physics* 42: (2009) 105201.
- [27] Pintassilgo, C. D., Loureiro, J. and Guerra, V., “Modelling of a  $N_2$ - $O_2$  flowing



- afterglow for plasma sterilization”, *Journal of Physics D: Applied Physics* 38: (2005) 417.
- [28] Pitaevskii, L. P. and Lifshitz, E. M., “Physical Kinetics: Volume 10”, Butterworth-Heinemann, 1981.
- [29] Pointu, A. M., Ricard, A., Dodet, B., Odic, E., Larbre, J. and Ganciu, M., “Production of active species in N<sub>2</sub>-O<sub>2</sub> flowing post-discharges at atmospheric pressure for sterilization”, *Journal of Physics D: Applied Physics* 38: (2005) 1905.
- [30] Scharfetter, D. L. and Gummel, H. K., “Large-signal analysis of a silicon Read diode oscillator”, *IEEE Transactions on Electron Devices* 16: (1969) 64.
- [31] Sègur, P. and Massines, F., 13th International Conference on Gas Discharges and Their Applications (Glasgow, 3–8 September): (2000) p 15.
- [32] Trunec, D., Brablec, A. and Buchta, J., “Atmospheric pressure glow discharge in neon”, *Journal of Applied Physics* 34: (2001) 1697.
- [33] Tepper, J. and Lindmayer, M., HAKONE VII (Greifswald, 10–13 Sept.) 1: (2000) 38.
- [34] Tochikubo, F., Uchida, S., Yasui, H. and Sato, K., “Numerical Simulation of NO Oxidation in Dielectric Barrier Discharge with Microdischarge Formation”, *Japanese Journal of Applied Physics* 48: (2009) 076507.
- [35] Tsai, I. H. and Hsu, C. C., “Numerical Simulation of Downstream Kinetics of an Atmospheric-Pressure Nitrogen Plasma Jet”, *IEEE Transactions on Plasma Science* 38: (2010) 3387.
- [36] Ventzek, P. L. G., Sommerer, T. J., Hoekstra, R. J. and Kushner, M. J., “Two dimensional hybrid model of inductively coupled plasma sources for etching”, *Applied Physics Letters* 63: (1993) 605.

Table 1: Subdivision of plasmas

Low-temperature plasma (LTP)		High-temperature plasma (HTP)
Thermal LTP	Nonthermal LTP	$T_i \approx T_e \geq 10^7 K$
$T_e \approx T_i \approx T_R \leq 2 \times 10^4 K$	$T_i \approx T_R \approx 300 K$ $T_i \ll T_e \leq 10^5 K$	
e.g., arc plasma at normal pressure	e.g., low-pressure glow discharge	e.g., fusion plasmas

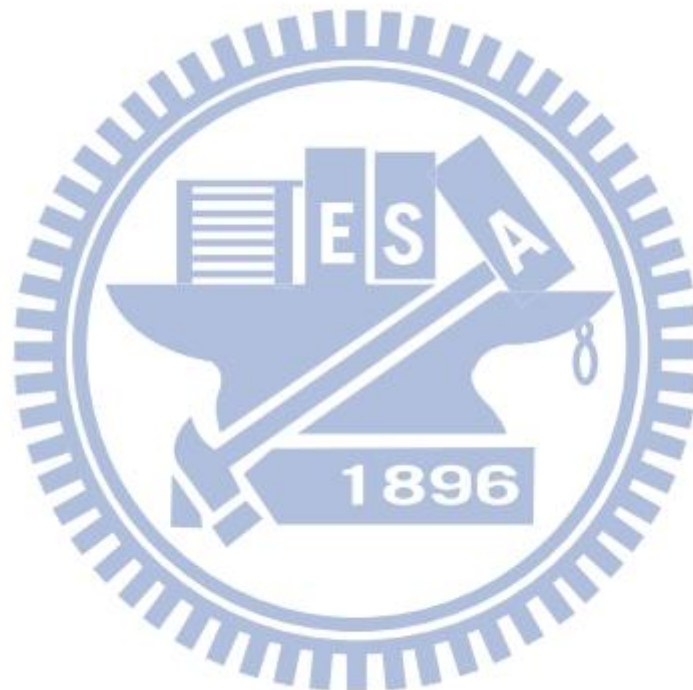


Table 2: Nitrogen Plasma Chemistry

No.	Reaction Channel	Threshold (eV)	Rate Coefficient
(1)	$e + N_2 \rightarrow e + N_2$	0.0	cross section
(2)	$e + N_2 \rightarrow 2e + N_2^+$	15.58	cross section
(3)	$e + N_2 \rightarrow e + N_2(\text{rot})$	0.02	cross section
(4)	$e + N_2 \rightarrow e + N_2(\text{res})$	0.29	cross section
(5)	$e + N_2 \rightarrow e + N_2(v=1)$	0.291	cross section
(6)	$e + N_2 \rightarrow e + N_2(v=2)$	0.59	cross section
(7)	$e + N_2 \rightarrow e + N_2(v=3)$	0.88	cross section
(8)	$e + N_2 \rightarrow e + N_2(v=4)$	1.17	cross section
(9)	$e + N_2 \rightarrow e + N_2(v=5)$	1.47	cross section
(10)	$e + N_2 \rightarrow e + N_2(v=6)$	1.76	cross section
(11)	$e + N_2 \rightarrow e + N_2(A^3\Sigma_u^+)$	6.17	cross section
(12)	$e + N_2 \rightarrow e + N_2(B^3\Pi_g)$	7.35	cross section
(13)	$e + N_2 \rightarrow e + N_2(a^1\Sigma_u^-)$	8.40	cross section
(14)	$e + N_2 \rightarrow e + N_2(C^3\Pi_u)$	11.03	cross section
(15)	$e + N_2 \rightarrow e + 2N$	12.00	$1.25 \times 10^{-16} \times (11608 \times T_e)^{0.49} \times \text{Exp}(-1.6 \times 10^5 / 11608 / T_e) m^3 s^{-1}$
(16)	$e + N_2^+ \rightarrow 2N$	0.0	$2.8 \times 10^{-13} (T_g / T_e)^{0.5} m^3 s^{-1}$
(17)	$e + N_2^+ \rightarrow N(^2D) + N$	0.0	$3.7 \times 10^{-13} m^3 s^{-1}$
(18)	$e + N_4^+ \rightarrow N_2(C^3\Pi_u) + N_2$	0.0	$2.0 \times 10^{-12} (T_g / T_e)^{0.5} m^3 s^{-1}$
(19)	$N_2^+ + N_2 + N_2 \rightarrow N_4^+ + N_2$	0.0	$5.0 \times 10^{-41} m^6 s^{-1}$
(20)	$N_2(a^1\Sigma_u^-) + N_2(A^3\Sigma_u^+) \rightarrow e + N_4^+$	0.0	$5.0 \times 10^{-17} m^3 s^{-1}$
(21)	$N_2(a^1\Sigma_u^-) + N_2(a^1\Sigma_u^-) \rightarrow e + N_4^+$	0.0	$2.0 \times 10^{-16} m^3 s^{-1}$
(22)	$N_2(A^3\Sigma_u^+) + N_2(A^3\Sigma_u^+) \rightarrow N_2(B^3\Pi_g) + N_2$	0.0	$7.7 \times 10^{-17} m^3 s^{-1}$

(23)	$N_2(A^3\Sigma_u^+) + N_2(A^3\Sigma_u^+) \rightarrow N_2(C^3\Pi_u) + N_2$	0.0	$3.0 \times 10^{-16} m^3 s^{-1}$
(24)	$N_2(B^3\Pi_g) + N_2 \rightarrow N_2(A^3\Sigma_u^+) + N_2$	0.0	$5.0 \times 10^{-17} m^3 s^{-1}$
(25)	$N_2(C^3\Pi_u) + N_2 \rightarrow N_2(a^1\Sigma_u^-) + N_2$	0.0	$1.0 \times 10^{-17} m^3 s^{-1}$
(26)	$N_2(a^1\Sigma_u^-) + N_2 \rightarrow N_2(B^3\Pi_g) + N_2$	0.0	$2.0 \times 10^{-19} m^3 s^{-1}$
(27)	$N_2(a^1\Sigma_u^-) + N_2 \rightarrow 2N_2$	0.0	$2.0 \times 10^{-19} m^3 s^{-1}$
(28)	$N + N + N_2 \rightarrow 2N_2$	0.0	$8.3 \times 10^{-46} \times \text{Exp}(500/T_g) m^6 s^{-1}$
(29)	$N + N + N_2 \rightarrow N_2(A^3\Sigma_u^+) + N_2$	0.0	$8.27 \times 10^{-46} \times \text{Exp}(500/T_g) m^6 s^{-1}$
(30)	$N + N + N_2 \rightarrow N_2(B^3\Pi_g) + N_2$	0.0	$8.3 \times 10^{-46} \times \text{Exp}(500/T_g) m^6 s^{-1}$
(31)	$N_2(A^3\Sigma_u^+) \rightarrow N_2 + h\nu 293nm$	0.0	$5.0 \times 10^{-1} s^{-1}$
(32)	$N_2(B^3\Pi_g) \rightarrow N_2(A^3\Sigma_u^+) + h\nu 1045nm$	0.0	$1.5 \times 10^5 s^{-1}$
(33)	$N_2(C^3\Pi_u) \rightarrow N_2(B^3\Pi_g) + h\nu 336.5nm$	0.0	$2.7 \times 10^7 s^{-1}$
(34)	$N_2(a^1\Sigma_u^-) \rightarrow N_2 + h\nu 177.1nm$	0.0	$1.0 \times 10^2 s^{-1}$

Table 3: N<sub>2</sub>/O<sub>2</sub> Plasma Chemistry

No.	Reaction Channel	Threshold (eV)	Rate Coefficient
(1)	$e + N_2 \rightarrow e + N_2$	0.0	cross section
(2)	$e + N_2 \rightarrow 2e + N_2^+$	15.58	cross section
(3)	$e + N_2 \rightarrow e + N_2(\text{rot})$	0.02	cross section
(4)	$e + N_2 \rightarrow e + N_2(\text{res})$	0.29	cross section
(5)	$e + N_2 \rightarrow e + N_2(v=1)$	0.291	cross section
(6)	$e + N_2 \rightarrow e + N_2(v=2)$	0.59	cross section
(7)	$e + N_2 \rightarrow e + N_2(v=3)$	0.88	cross section
(8)	$e + N_2 \rightarrow e + N_2(v=4)$	1.17	cross section
(9)	$e + N_2 \rightarrow e + N_2(v=5)$	1.47	cross section
(10)	$e + N_2 \rightarrow e + N_2(v=6)$	1.76	cross section
(11)	$e + N_2 \rightarrow e + N_2(A^3\Sigma_u^+)$	6.17	cross section
(12)	$e + N_2 \rightarrow e + N_2(B^3\Pi_g)$	7.35	cross section
(13)	$e + N_2 \rightarrow e + N_2(a^1\Sigma_u^-)$	8.40	cross section
(14)	$e + N_2 \rightarrow e + N_2(C^3\Pi_u)$	11.03	cross section
(15)	$e + N_2 \rightarrow e + 2N$	12.0	$1.25 \times 10^{-16} \times (11608 \times T_e)^{0.49} \times \text{Exp}(-1.6 \times 10^5 / 11608 / T_e) m^3 s^{-1}$
(16)	$e + O_2 \rightarrow e + O_2$	0.0	cross section
(17)	$e + O_2 \rightarrow 2e + O_2^+$	12.06	cross section
(18)	$e + O_2 \rightarrow O^- + O$	0.0	cross section
(19)	$e + O_2 + O_2 \rightarrow O_2^- + O_2$	0.0	cross section
(20)	$e + O_2 \rightarrow e + O_2(a)$	0.977	cross section
(21)	$e + O_2 \rightarrow e + 2O$	6.0	cross section
(22)	$e + O_2 \rightarrow e + O + O(^1D)$	8.4	cross section
(23)	$e + O_2 \rightarrow e + O + O(^1S)$	10.0	cross section
(24)	$e + N_2^+ \rightarrow N(^2D) + N$	0.0	$3.7 \times 10^{-13} m^3 s^{-1}$
(25)	$e + N_2^+ \rightarrow 2N$	0.0	$2.8 \times 10^{-13} (T_g/T_e)^{0.5} m^3 s^{-1}$

(26)	$e + N_4^+ \rightarrow N_2(C^3\Pi_u) + N_2$	0.0	$2.0 \times 10^{-12} (T_g/T_e)^{0.5} m^3 s^{-1}$
(27)	$e + O_2^+ \rightarrow O(^1D) + O$	0.0	$2.1 \times 10^{-13} m^3 s^{-1}$
(28)	$N_2(a^1\Sigma_u^-) + N_2(A^3\Sigma_u^+) \rightarrow e + N_4^+$	0.0	$5.0 \times 10^{-17} m^3 s^{-1}$
(29)	$N_2(a^1\Sigma_u^-) + N_2(a^1\Sigma_u^-) \rightarrow e + N_4^+$	0.0	$2.0 \times 10^{-16} m^3 s^{-1}$
(30)	$N_2^+ + N_2 + N_2 \rightarrow N_4^+ + N_2$	0.0	$5.0 \times 10^{-41} m^6 s^{-1}$
(31)	$N_2^+ + O^- \rightarrow N_2 + O$	0.0	$7.8 \times 10^{-12} m^3 s^{-1}$
(32)	$O_2^+ + O_2^- \rightarrow 2O_2$	0.0	$7.8 \times 10^{-12} m^3 s^{-1}$
(33)	$O_2^+ + O^- \rightarrow O_2 + O$	0.0	$7.5 \times 10^{-12} m^3 s^{-1}$
(34)	$O_2^- + O_2(a) \rightarrow e + 2O_2$	0.0	$2.0 \times 10^{-16} m^3 s^{-1}$
(35)	$O_2^- + O \rightarrow e + O_3$	0.0	$1.5 \times 10^{-16} m^3 s^{-1}$
(36)	$O_2^- + N_2(A^3\Sigma_u^+) \rightarrow e + O_2 + N_2$	0.0	$2.1 \times 10^{-15} m^3 s^{-1}$
(37)	$O_2^- + N_2(B^3\Pi_g) \rightarrow e + O_2 + N_2$	0.0	$2.5 \times 10^{-15} m^3 s^{-1}$
(38)	$O^- + O_2(a) \rightarrow e + O_3$	0.0	$3.0 \times 10^{-16} m^3 s^{-1}$
(39)	$O^- + N_2(A^3\Sigma_u^+) \rightarrow e + O + N_2$	0.0	$2.2 \times 10^{-15} m^3 s^{-1}$
(40)	$O^- + N_2(B^3\Pi_g) \rightarrow e + O + N_2$	0.0	$1.9 \times 10^{-15} m^3 s^{-1}$
(41)	$O^- + O \rightarrow e + O_2$	0.0	$5.0 \times 10^{-16} m^3 s^{-1}$
(42)	$O^- + N \rightarrow e + NO$	0.0	$2.6 \times 10^{-16} m^3 s^{-1}$
(43)	$O^- + O_2 \rightarrow e + O_3$	0.0	$5.0 \times 10^{-21} m^3 s^{-1}$
(44)	$N + O + N_2 \rightarrow NO + N_2$	0.0	$1.76 \times 10^{-43} \times T_g^{-0.5} m^6 s^{-1}$
(45)	$O + O_2 + N_2 \rightarrow O_3 + N_2$	0.0	$5.6 \times 10^{-46} m^6 s^{-1}$
(46)	$N_2(A^3\Sigma_u^+) + N_2(A^3\Sigma_u^+) \rightarrow N_2(B^3\Pi_g) + N_2$	0.0	$7.7 \times 10^{-17} m^3 s^{-1}$
(47)	$N_2(A^3\Sigma_u^+) + N_2(A^3\Sigma_u^+) \rightarrow N_2(C^3\Pi_u) + N_2$	0.0	$3.0 \times 10^{-16} m^3 s^{-1}$
(48)	$N_2(A^3\Sigma_u^+) + O_2 \rightarrow 2O + N_2$	0.0	$1.7 \times 10^{-18} m^3 s^{-1}$

(49)	$N_2(A^3\Sigma_u^+) + O_2 \rightarrow O_2(a) + N_2$	0.0	$7.5 \times 10^{-19} m^3 s^{-1}$
(50)	$N_2(A^3\Sigma_u^+) + O \rightarrow N(^2D) + NO$	0.0	$7.0 \times 10^{-19} m^3 s^{-1}$
(51)	$N_2(A^3\Sigma_u^+) + O \rightarrow O(^1S) + N_2$	0.0	$2.1 \times 10^{-17} m^3 s^{-1}$
(52)	$N_2(B^3\Pi_g) + N_2 \rightarrow N_2(A^3\Sigma_u^+) + N_2$	0.0	$5.0 \times 10^{-17} m^3 s^{-1}$
(53)	$N_2(B^3\Pi_g) + O_2 \rightarrow 2O + N_2$	0.0	$1.1 \times 10^{-16} m^3 s^{-1}$
(54)	$N_2(a^1\Sigma_u^-) + N_2 \rightarrow N_2(B^3\Pi_g) + N_2$	0.0	$2.0 \times 10^{-19} m^3 s^{-1}$
(55)	$N_2(a^1\Sigma_u^-) + N_2 \rightarrow 2N_2$	0.0	$2.0 \times 10^{-19} m^3 s^{-1}$
(56)	$N_2(a^1\Sigma_u^-) + O_2 \rightarrow 2O + N_2$	0.0	$2.8 \times 10^{-17} m^3 s^{-1}$
(57)	$N_2(a^1\Sigma_u^-) + NO \rightarrow O + N + N_2$	0.0	$3.6 \times 10^{-16} m^3 s^{-1}$
(58)	$N_2(C^3\Pi_u) + N_2 \rightarrow N_2(a^1\Sigma_u^-) + N_2$	0.0	$1.0 \times 10^{-17} m^3 s^{-1}$
(59)	$N_2(C^3\Pi_u) + O_2 \rightarrow N_2 + O + O(^1S)$	0.0	$3.0 \times 10^{-16} m^3 s^{-1}$
(60)	$N(^2D) + O_2 \rightarrow NO + O$	0.0	$1.5 \times 10^{-18} \times (T_g/300)^{0.5} m^3 s^{-1}$
(61)	$N(^2D) + O_2 \rightarrow NO + O(^1D)$	0.0	$6.0 \times 10^{-18} m^3 s^{-1}$
(62)	$O(^1D) + O_2 \rightarrow O + O_2(a)$	0.0	$3.4 \times 10^{-17} m^3 s^{-1}$
(63)	$O(^1D) + O_2 \rightarrow O + O_2$	0.0	$6.4 \times 10^{-18} \times \text{Exp}(67/T_g) m^3 s^{-1}$
(64)	$N_2(A^3\Sigma_u^+) + NO \rightarrow NO(A) + N_2$	0.0	$6.6 \times 10^{-17} m^3 s^{-1}$
(65)	$NO(A^2\Sigma^+) + N_2 \rightarrow NO + N_2$	0.0	$1.0 \times 10^{-19} m^3 s^{-1}$
(66)	$NO(A^2\Sigma^+) + O_2 \rightarrow NO + O_2$	0.0	$1.5 \times 10^{-16} m^3 s^{-1}$
(67)	$NO(A^2\Sigma^+) + NO \rightarrow 2NO$	0.0	$2.0 \times 10^{-16} m^3 s^{-1}$
(68)	$N + O + N_2 \rightarrow NO(B^2\Pi) + N_2$	0.0	$2.9 \times 10^{-46} m^6 s^{-1}$
(69)	$NO(B^2\Pi) + N_2 \rightarrow NO + N_2$	0.0	$6.1 \times 10^{-19} m^3 s^{-1}$
(70)	$O(^1S) + N_2 + N_2 \rightarrow O(^1S)N_2 + N_2$	0.0	$2.0 \times 10^{-48} m^6 s^{-1}$
(71)	$O(^1S)N_2 + N_2 \rightarrow O(^1S) + N_2 + N_2$	0.0	$5.0 \times 10^{-18} m^3 s^{-1}$

(72)	$N + NO \rightarrow O + N_2$	0.0	$1.05 \times 10^{-18} \times T_g^{0.5} m^3 s^{-1}$
(73)	$N_2(B^3\Pi_g) + NO \rightarrow N_2(A^3\Sigma_u^+) + NO$	0.0	$2.4 \times 10^{-16} m^3 s^{-1}$
(74)	$N + N + N_2 \rightarrow 2N_2$	0.0	$8.3 \times 10^{-46} \times \text{Exp}(500 / T_g) m^6 s^{-1}$
(75)	$N + N + N_2 \rightarrow N_2(A^3\Sigma_u^+) + N_2$	0.0	$8.27 \times 10^{-46} \times \text{Exp}(500 / T_g) m^6 s^{-1}$
(76)	$N + N + N_2 \rightarrow N_2(B^3\Pi_g) + N_2$	0.0	$8.3 \times 10^{-46} \times \text{Exp}(500 / T_g) m^6 s^{-1}$
(77)	$N + O_3 \rightarrow NO + O_2$	0.0	$2.0 \times 10^{-22} m^3 s^{-1}$
(78)	$O + O_3 \rightarrow O_2 + O_2$	0.0	$2.0 \times 10^{-17} \times \text{Exp}(-2300 / T_g) m^3 s^{-1}$
(79)	$N_2(B^3\Pi_g) \rightarrow N_2(A^3\Sigma_u^+) + h\nu 1045 nm$	0.0	$1.5 \times 10^5 s^{-1}$
(80)	$N_2(C^3\Pi_u) \rightarrow N_2(B^3\Pi_g) + h\nu 336 nm$	0.0	$2.7 \times 10^7 s^{-1}$
(81)	$N_2(a^1\Sigma_u^-) \rightarrow N_2 + h\nu 177 nm$	0.0	$1.0 \times 10^2 s^{-1}$
(82)	$N_2(A^3\Sigma_u^+) \rightarrow N_2 + h\nu 293 nm$	0.0	$5.0 \times 10^{-1} s^{-1}$
(83)	$NO(A^2\Sigma^+) \rightarrow NO + (180 \sim 260) nm$	0.0	$5.0 \times 10^6 s^{-1}$
(84)	$NO(B^2\Pi) \rightarrow NO + (260 \sim 380) nm$	0.0	$5.0 \times 10^5 s^{-1}$
(85)	$O(^1S)N_2 \rightarrow O(^1D) + N_2 + h\nu 557.7 nm$	0.0	$1.0 \times 10^7 s^{-1}$



Table 4: Cycle average in different mesh number test

<b>Mesh number (cells/mm)</b>	<b>Average Electron Density (#/m<sup>3</sup>)</b>	<b>Average N<sub>2</sub><sup>+</sup> Density (#/m<sup>3</sup>)</b>	<b>Average N<sub>4</sub><sup>+</sup> Density (#/m<sup>3</sup>)</b>	<b>Average N<sub>2</sub>(A<sup>3</sup>) Density (#/m<sup>3</sup>)</b>	<b>Average N<sub>2</sub>(B<sup>3</sup>) Density (#/m<sup>3</sup>)</b>	<b>Average N<sub>2</sub>(a<sup>1</sup>) Density (#/m<sup>3</sup>)</b>	<b>Average N<sub>2</sub>(C<sup>3</sup>) Density (#/m<sup>3</sup>)</b>	<b>Average Te (eV)</b>
<b>50 cells</b>	1.02E+14	9.34E+15	1.47E+15	8.44E+19	3.82E+15	5.40E+17	2.05E+16	3.01
<b>100 cells</b>	1.06E+14	9.83E+15	1.48E+15	8.39E+19	3.86E+15	5.42E+17	2.07E+16	3.15
<b>200 cells</b>	1.08E+14	1.01E+16	1.46E+15	8.37E+19	3.88E+15	5.41E+17	2.07E+16	3.24
<b>400 cells</b>	1.09E+14	1.02E+16	1.45E+15	8.36E+19	3.88E+15	5.40E+17	2.08E+16	3.27
<b>800 cells</b>	1.10E+14	1.03E+16	1.44E+15	8.35E+19	3.87E+15	5.39E+17	2.08E+16	3.28
<b>1000 cells</b>	1.10E+14	1.03E+16	1.44E+15	8.35E+19	3.87E+15	5.38E+17	2.08E+16	3.29

Table 5: Comparison of average absorbed power for varying applied voltage of 6200, 6600, 6800, 8600 V in a 60 kHz cycle, and a fixed gap distance of 0.5 mm.

<b>voltage</b>	electron absorbed (W/cm <sup>3</sup> )	N <sub>2</sub> <sup>+</sup> absorbed (W/cm <sup>3</sup> )	N <sub>4</sub> <sup>+</sup> absorbed (W/cm <sup>3</sup> )	Total absorbed (W/cm <sup>3</sup> )
<b>6200</b>	1.40	0.035	15.65	17.09
<b>6600</b>	4.99	0.076	40.11	45.18
<b>6800</b>	5.35	0.091	46.48	51.92
<b>8600</b>	21.39	0.244	121.98	143.61

Table 6: At 6200 V applied voltage and 60 kHz frequency, the compared of average number density, electron temperature and total absorbed power in different ceramic dielectric thickness (1.0 and 2.0 mm).

<b>dielectric thickness</b>	electron density (#/m <sup>3</sup> )	N <sub>2</sub> <sup>+</sup> density (#/m <sup>3</sup> )	N <sub>4</sub> <sup>+</sup> density (#/m <sup>3</sup> )	N <sub>2</sub> (A <sup>3</sup> ) density (#/m <sup>3</sup> )	N <sub>2</sub> (a <sup>1</sup> ) density (#/m <sup>3</sup> )	electron absorbed (W/cm <sup>3</sup> )	N <sub>2</sub> <sup>+</sup> absorbed (W/cm <sup>3</sup> )	N <sub>4</sub> <sup>+</sup> absorbed (W/cm <sup>3</sup> )
<b>1 mm</b>	6.08E14	1.68E13	8.15E16	6.47E19	3.80E17	21.99	0.213	119.80
<b>2 mm</b>	3.04E13	4.91E12	2.49E16	1.97E19	7.01E16	1.40	0.035	15.65

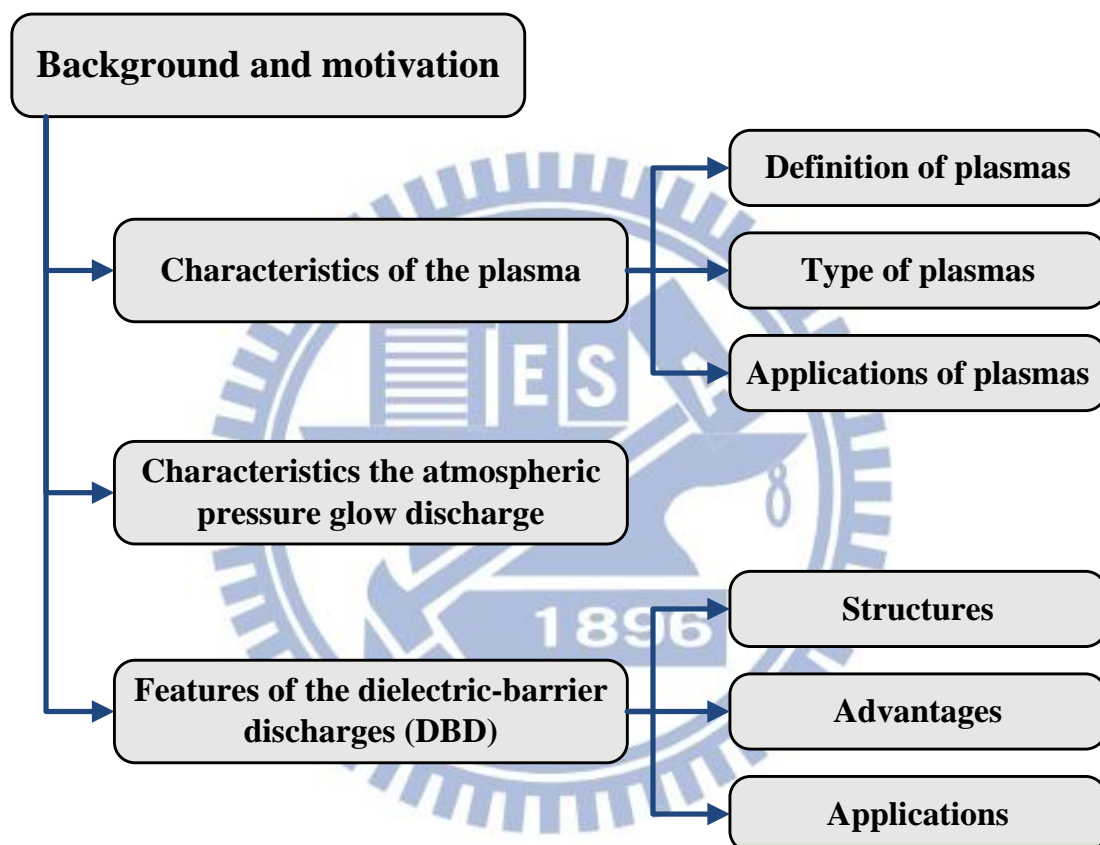


Figure 1. 1: The frame work of background and motivation

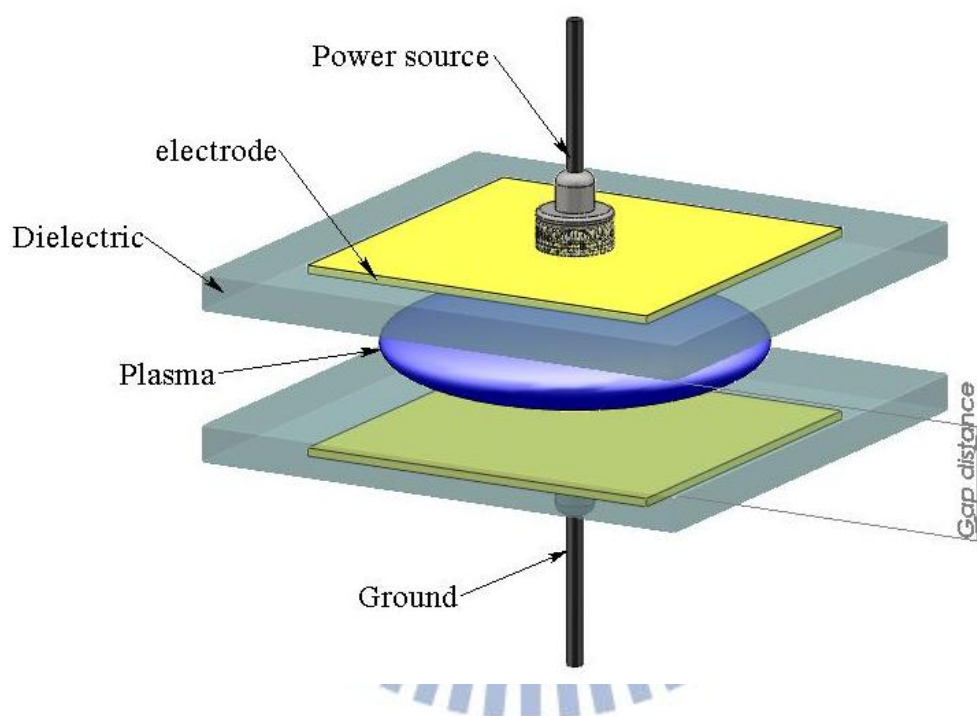


Figure 1. 2: Sketch of dielectric barrier discharge

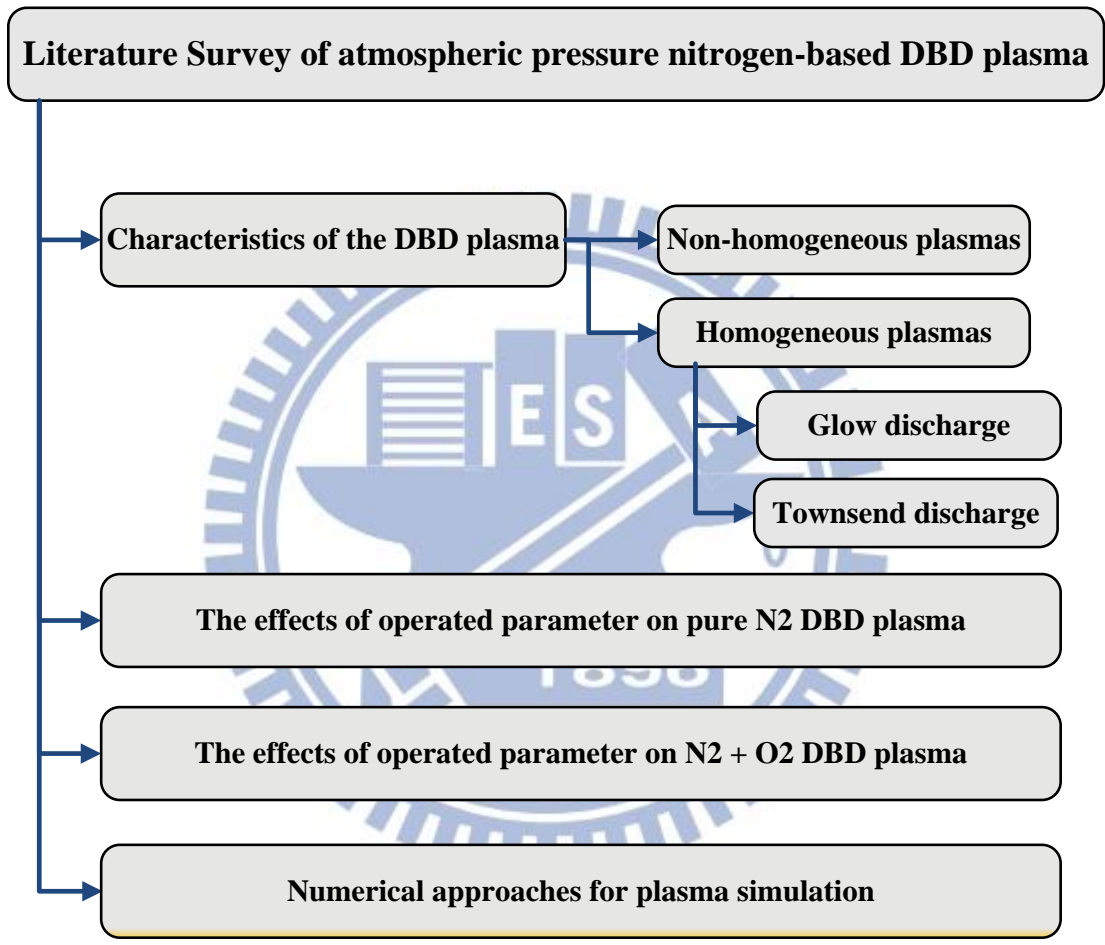


Figure 1. 3: The frame work of literature survey

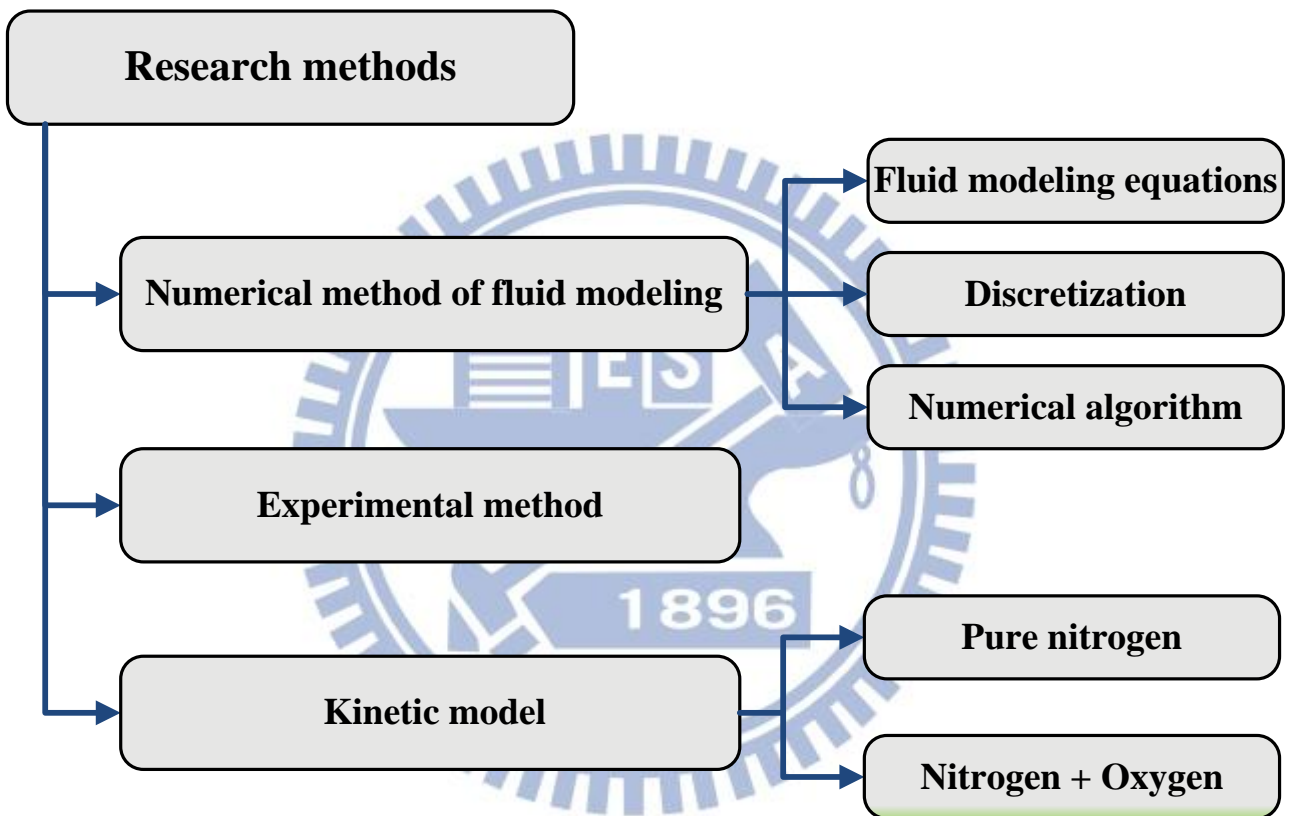


Figure 2. 1: The frame work of research methods

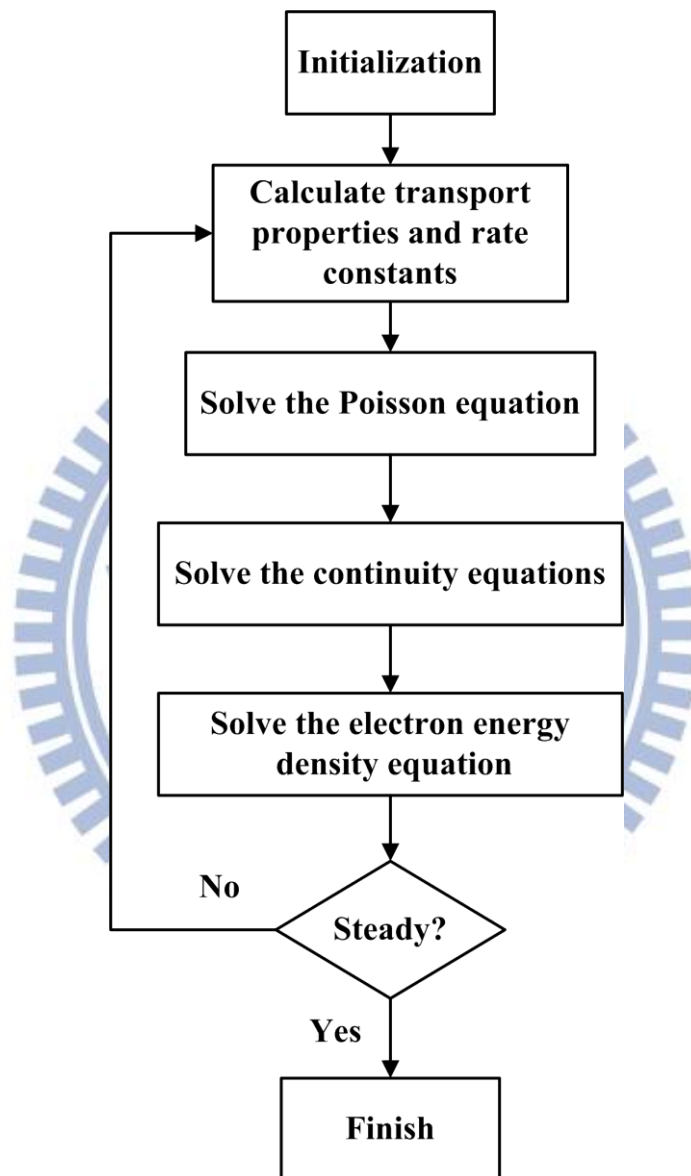


Figure 2. 2: The flowchart of plasma fluid modeling

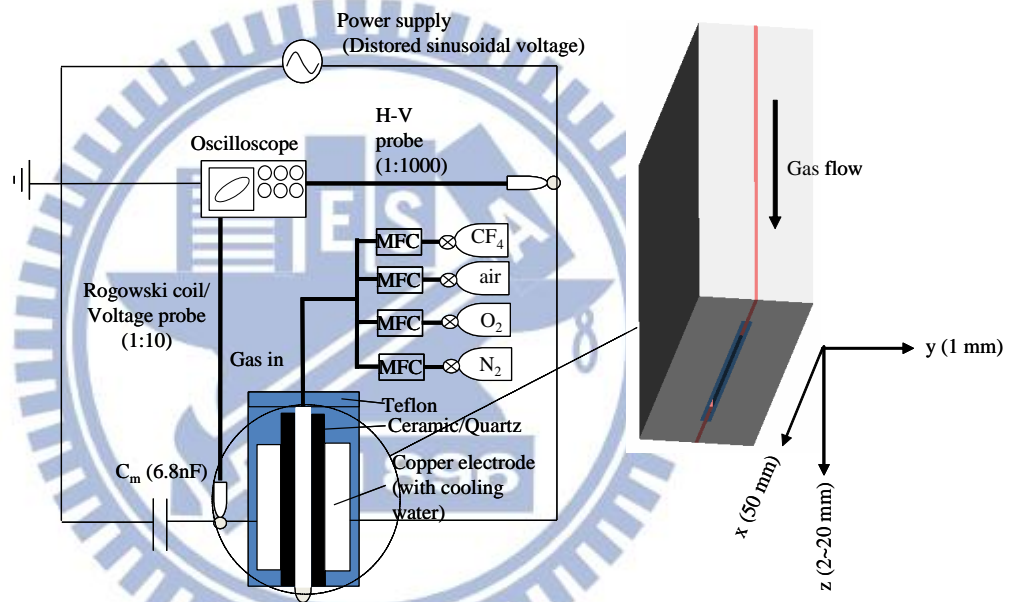


Figure 2. 3: Schematic sketch of a planar DBD APPJ



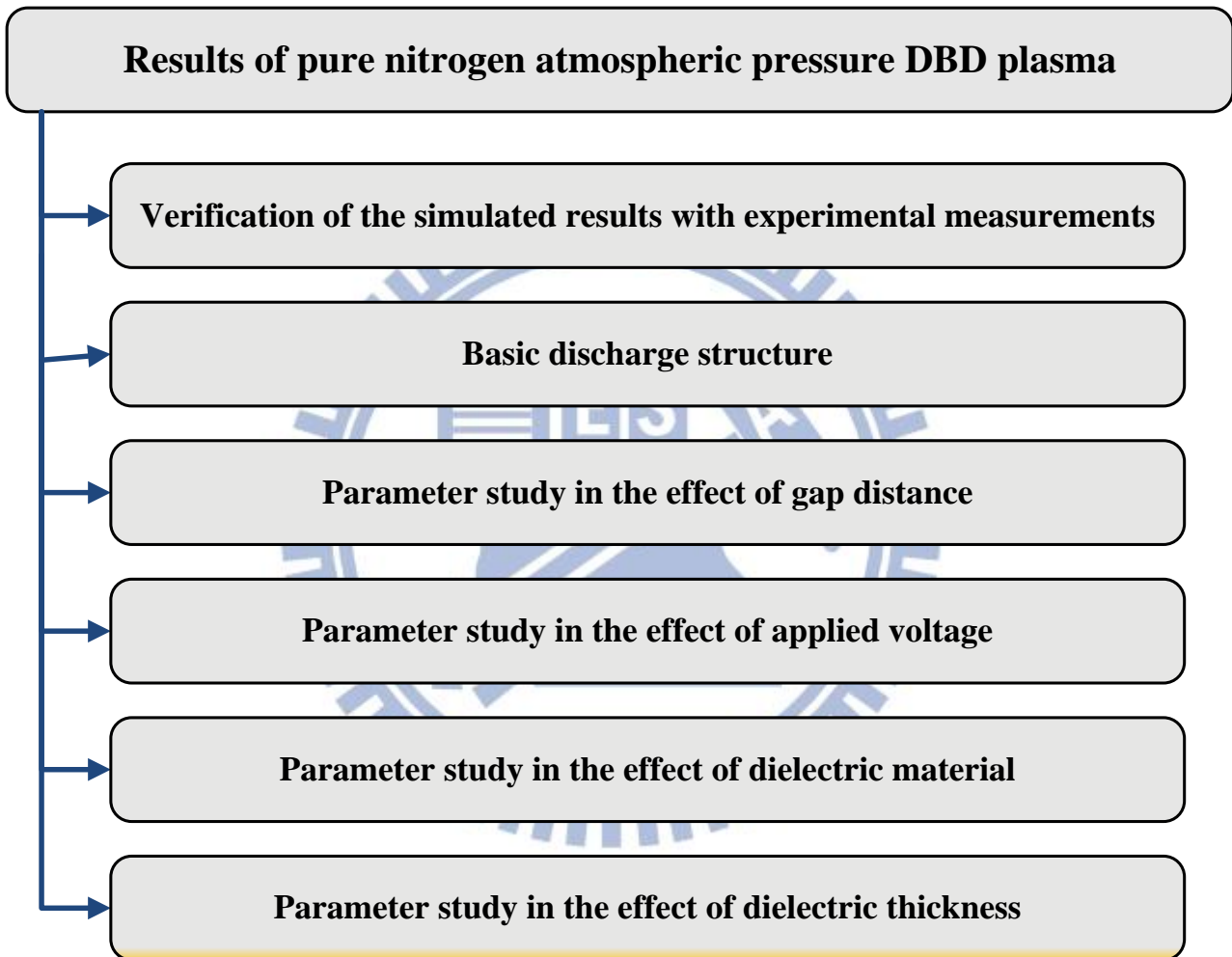


Figure 3. 1: The frame work of pure nitrogen results and discussions

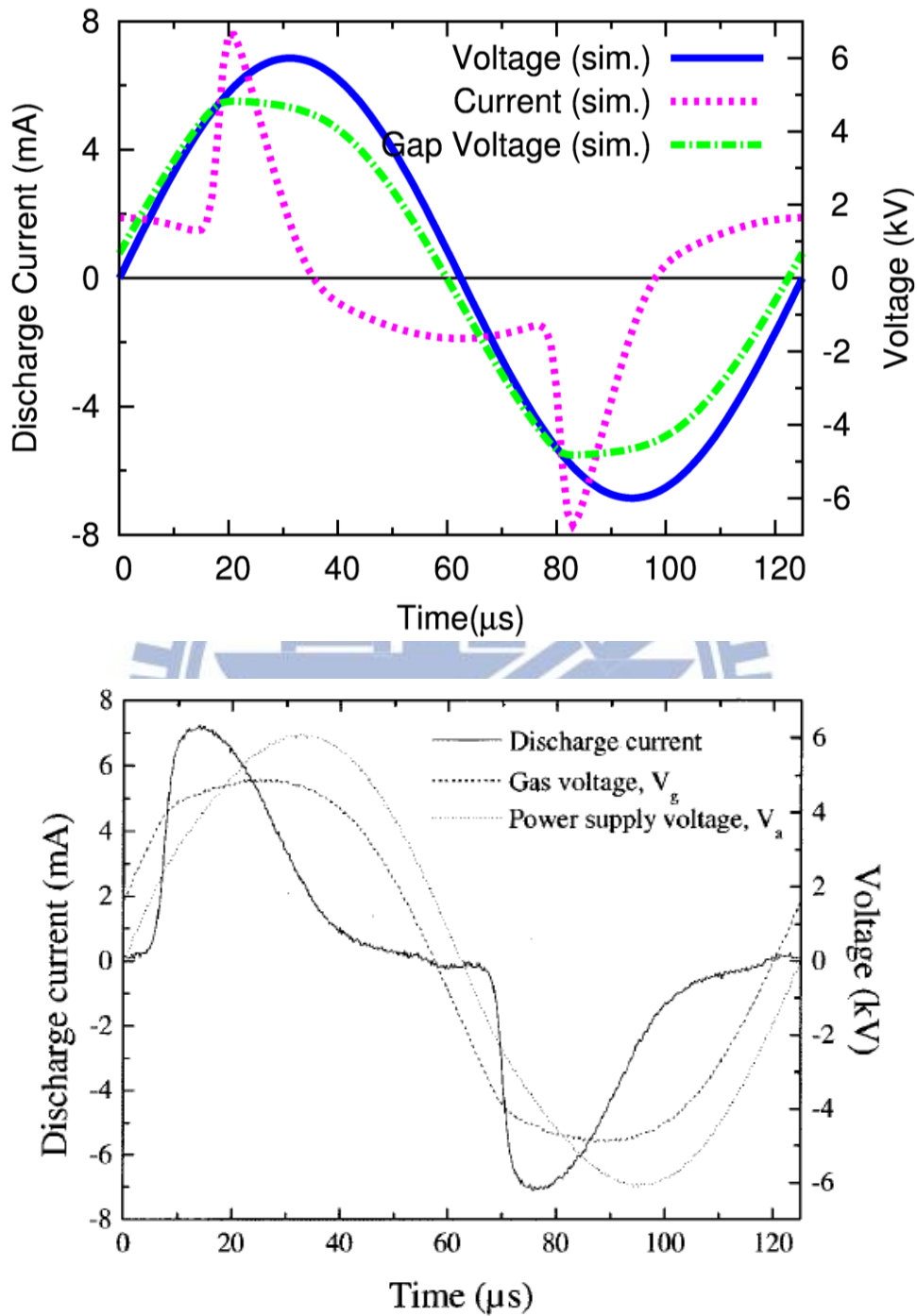


Figure 3. 2: Comparison of simulated (upper) and [Gherardi's *et al.*, 2001] experimental (bottom) voltages and currents for atmospheric pressure discharge using sinusoidal 8 kHz power source.

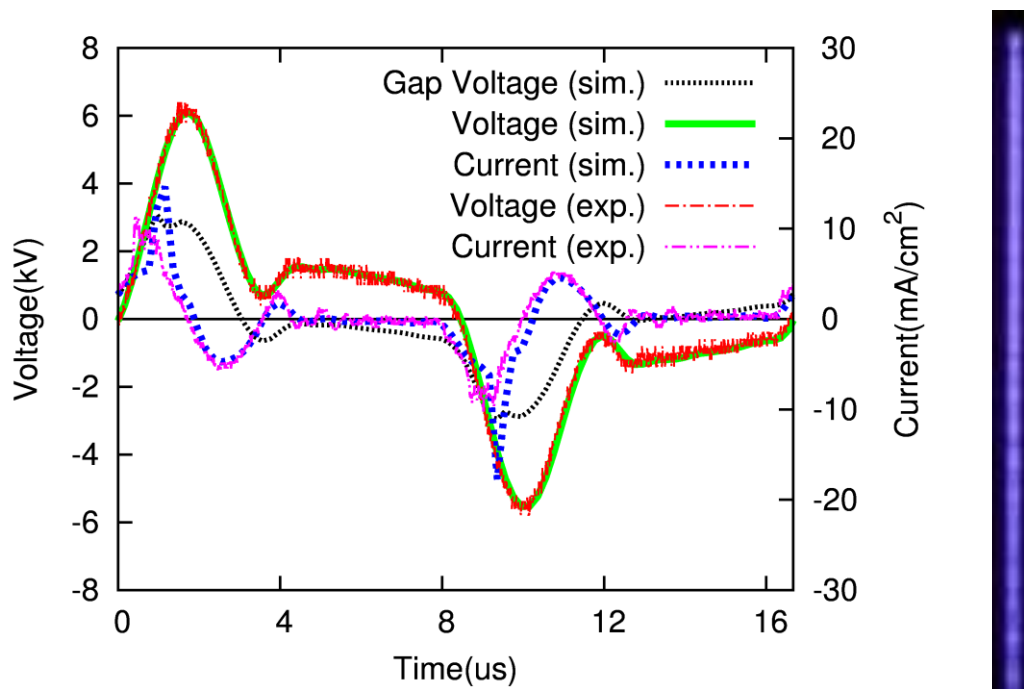


Figure 3. 3: Comparison of simulated and experimented current-voltage characteristic with voltage 6600 V and frequency 60 kHz. The distance between the two dielectric layers is 0.5 mm and the dielectric is 2.0 mm alumina. The photo image of discharge acquired by 0.2 second exposed time was at the right.

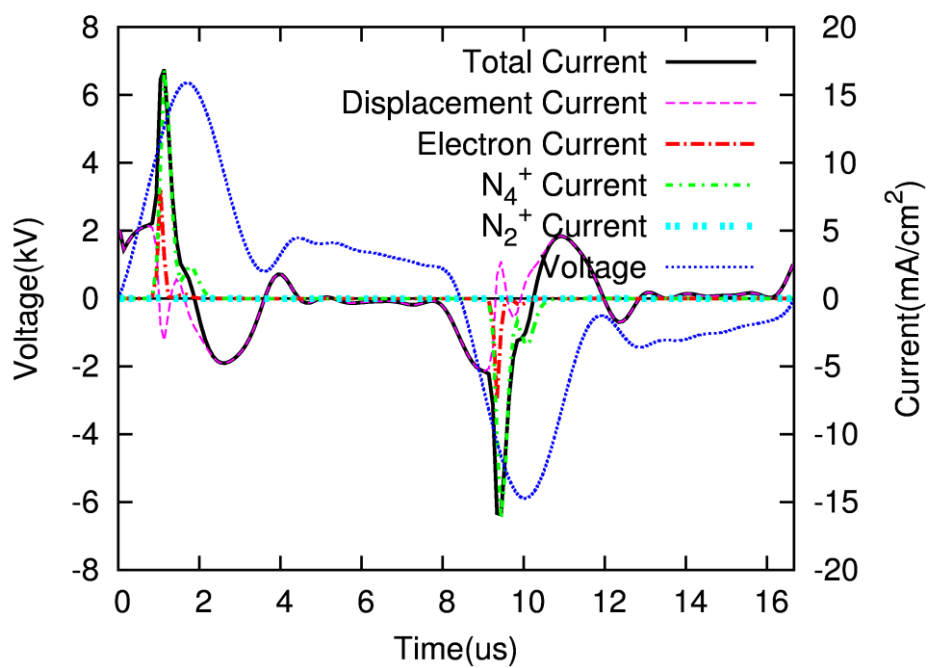


Figure 3. 4: Distributions of various discharge currents during a cycle via numerical modeling. The gap distance is 0.5 mm and using 2.0 mm thickness alumina dielectric. The applied voltage is 6600 V and 60 kHz frequency.

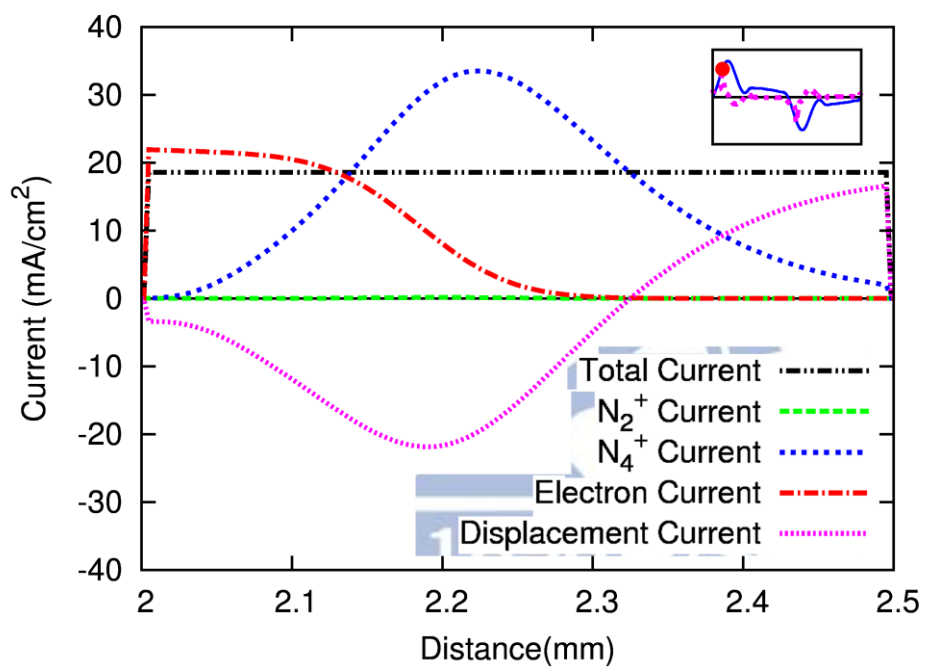


Figure 3. 5: Distributions of various discharge currents at the maximum discharge current via numerical modeling. The gap distance is 0.5 mm and using 2.0 mm thickness alumina dielectric. The applied voltage is 6600 V and 60 kHz frequency.

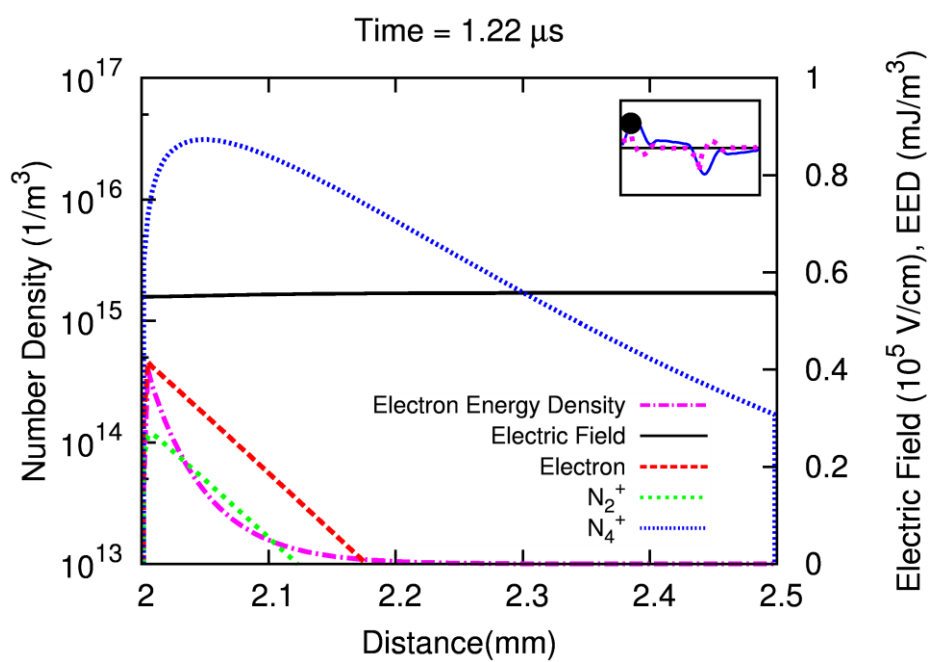


Figure 3. 6: Spatial distributions of electric field, charged particles and electron energy density at the time of maximum discharge current ( $0.86 \mu\text{s}$ ) between two alumina dielectric. The operating conditions are the same as in Figure 3. 3.

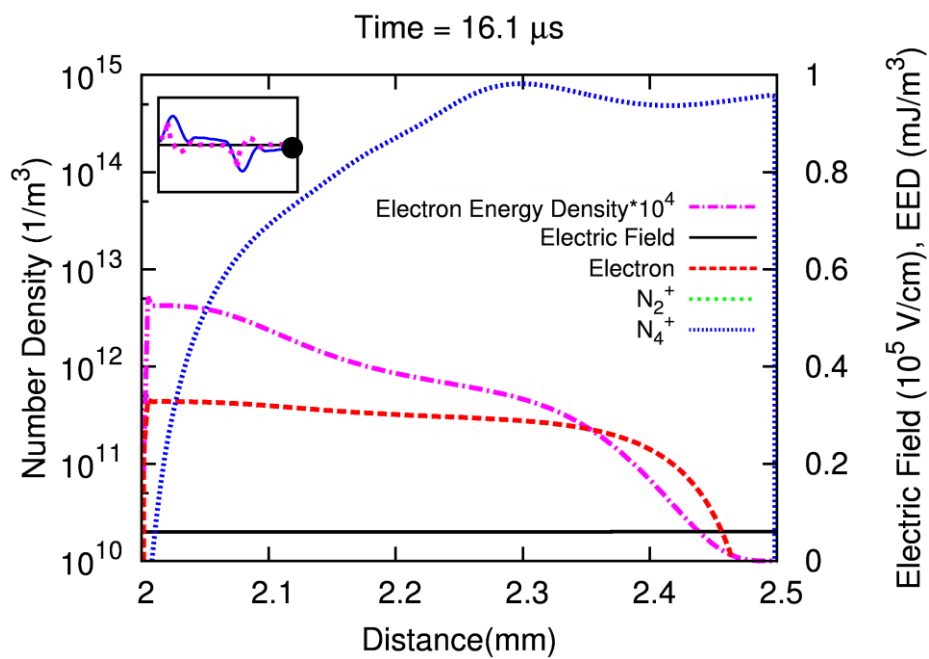


Figure 3. 7: Spatial distributions of electric field, charged particles and electron energy density at 15.5  $\mu$ s (after the breakdown) between two alumina dielectric. The operating conditions are the same as in Figure 3. 3.

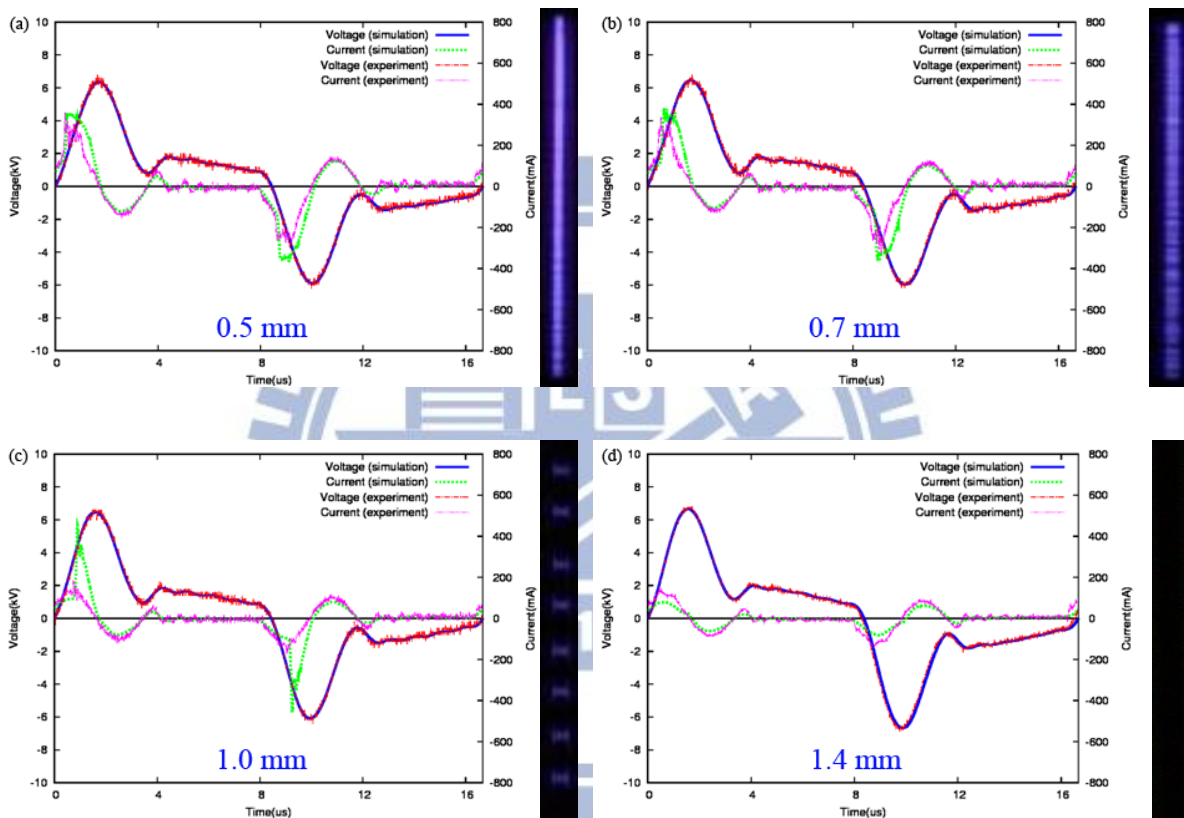


Figure 3. 8: Comparison of different gap distance (a) 0.5 mm (b) 0.7 mm (c) 1.0 mm (d) 1.4 mm discharged currents along with photo images of discharge at the right.



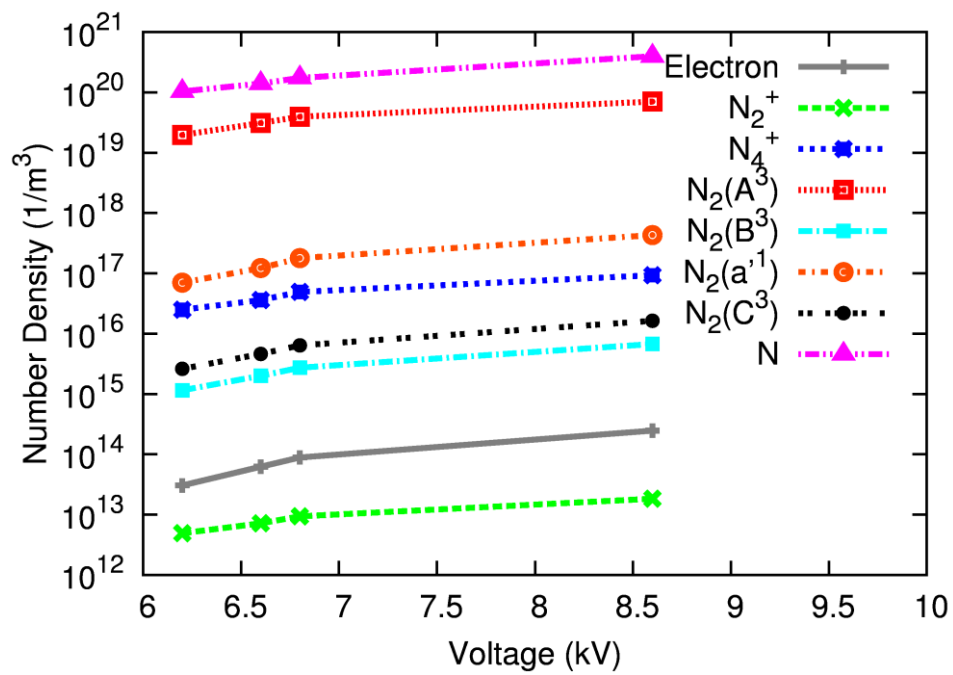


Figure 3. 9: Cycle-space averaged number densities of various species in nitrogen DBD for varying applied voltage of 6200, 6600, 6800, 8600 V, and a fixed gap distance of 0.5 mm. The alumina dielectric thickness is 2.0 mm and frequency is 60 kHz for all cases.

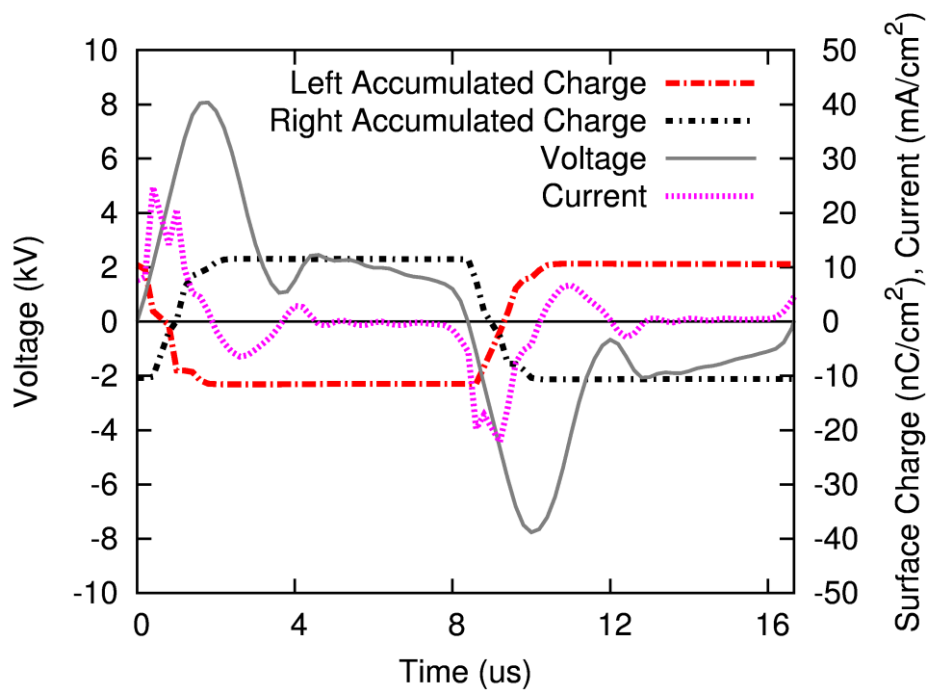


Figure 3. 10: Simulated current, gap voltage, applied voltage and accumulated charges at dielectric surfaces using 2.0 mm ceramic. The applied peak voltage is 8600 V and frequency is 60 kHz. The gap distance between dielectric is kept 0.5 mm.

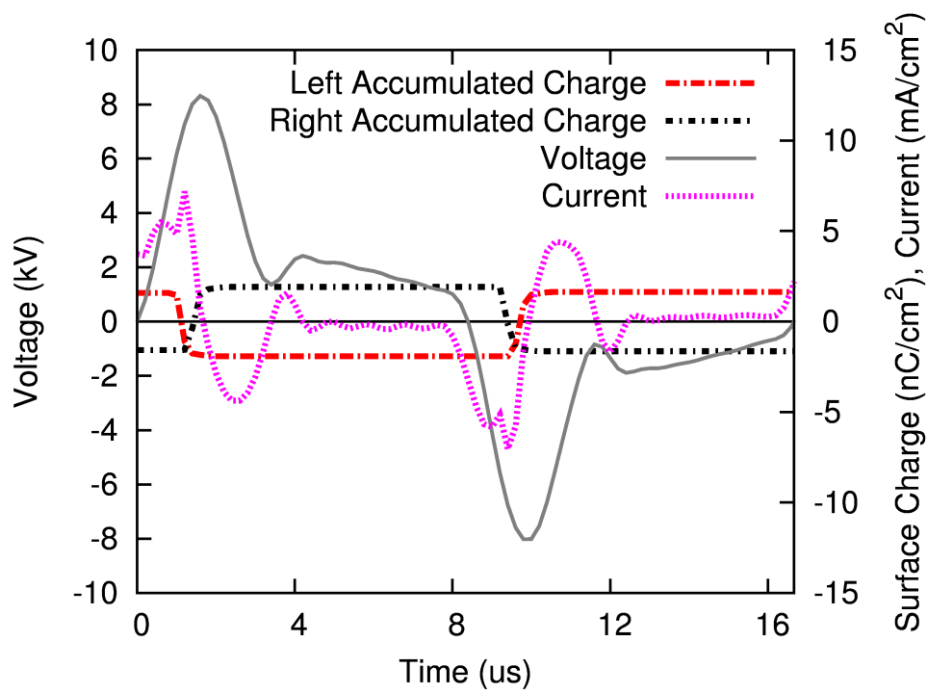


Figure 3. 11: Simulated current, gap voltage, applied voltage and accumulated charges at dielectric surfaces using 2.0 mm quartz. The applied peak voltage is 8600 V and frequency is 60 kHz. The gap distance between dielectric is kept 0.5 mm.

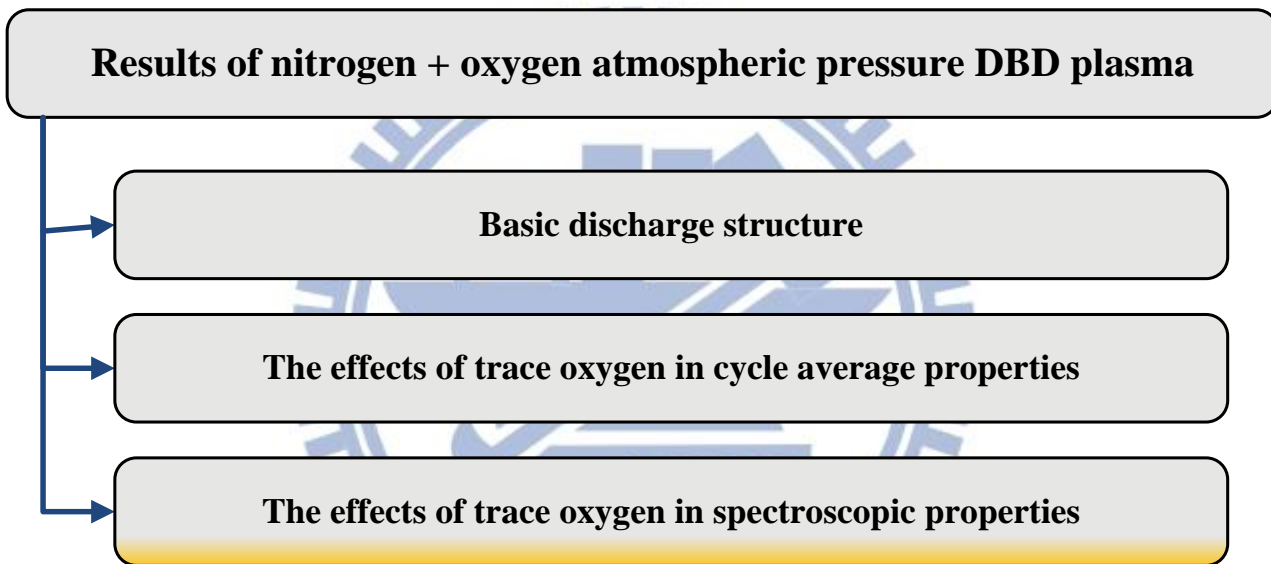


Figure 4. 1: The frame work of oxygen addition on nitrogen-based results and discussions

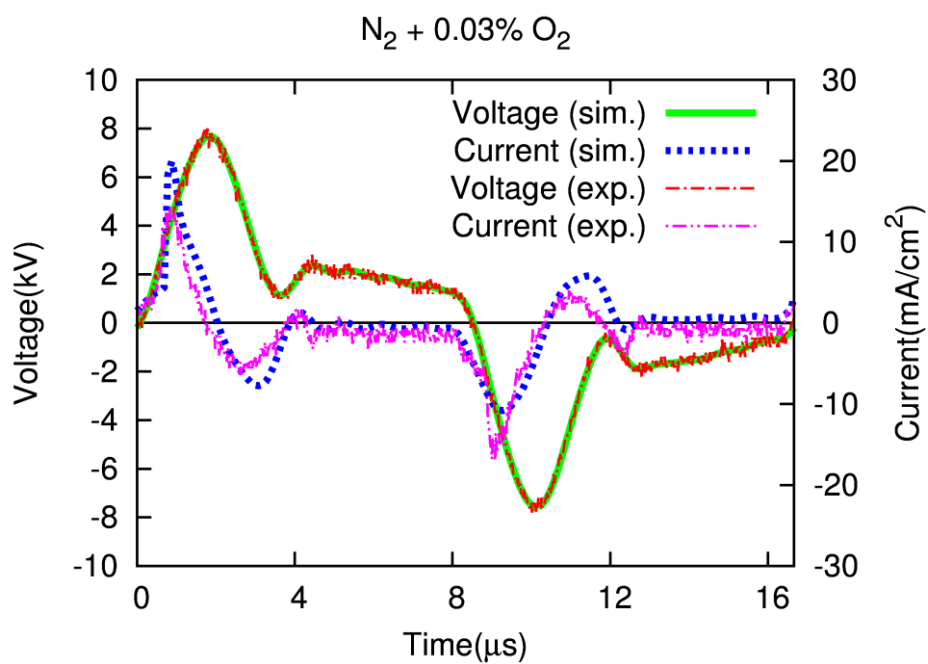


Figure 4. 2: Comparison of simulated and experimented of  $N_2$  with 0.03%  $O_2$  current-voltage characteristic with voltage 8200 V and frequency 60 kHz. The distance between the two dielectric layers is 1.0 mm and the dielectric is 1.0 mm quartz.

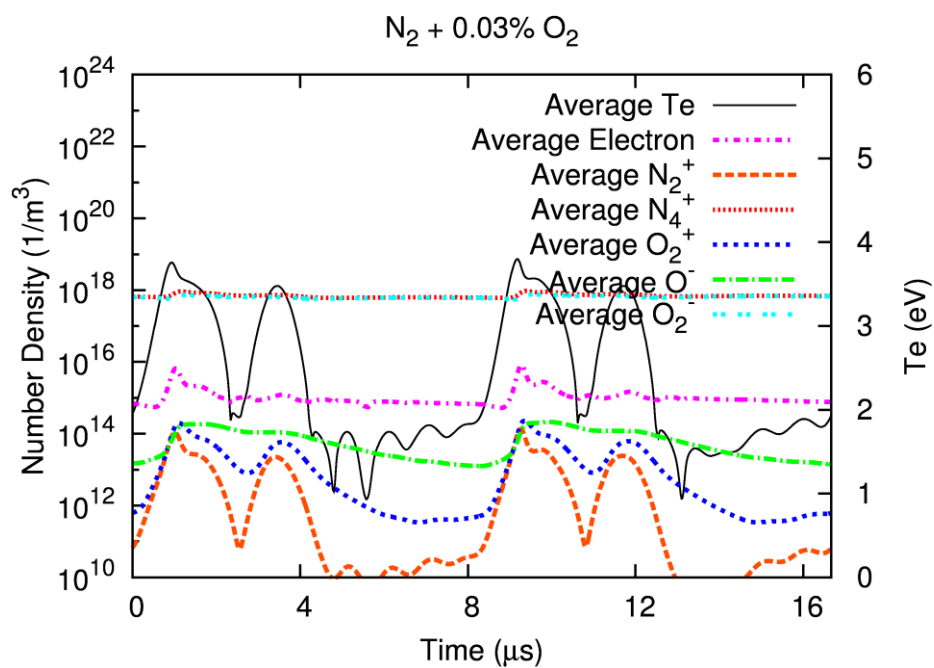


Figure 4. 3: Distributions of various spatial-average densities for charge species in  $N_2 + 0.03\% O_2$  DBD. The applied peak voltage is 8200 V and frequency is 60 kHz. The gap distance between quartz dielectric is 1.0 mm.

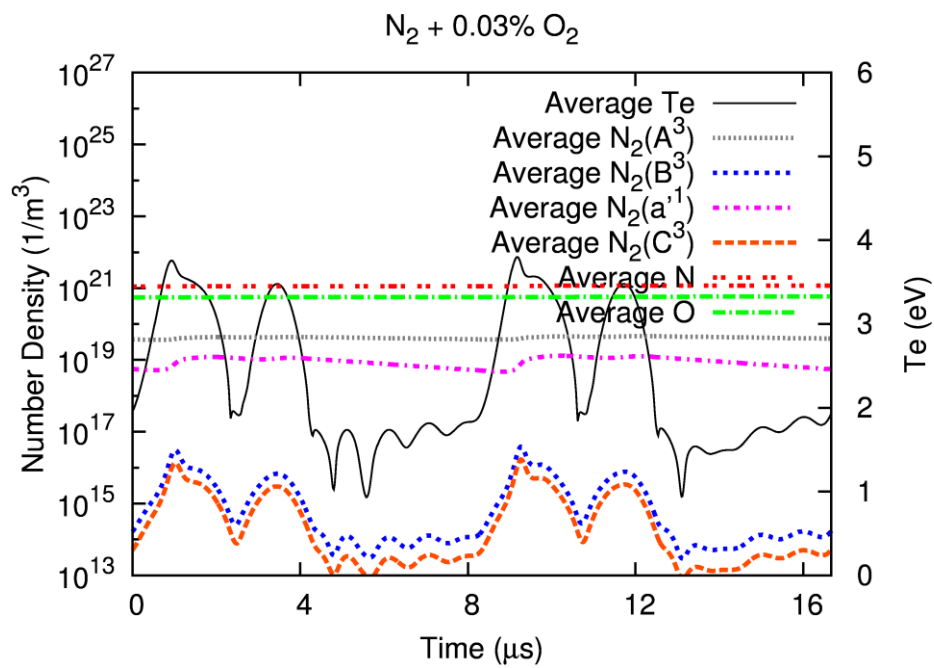


Figure 4. 4: Distributions of various spatial-average densities for neutral species in  $N_2 + 0.03\% O_2$  DBD. The applied peak voltage is 8200 V and frequency is 60 kHz. The gap distance between quartz dielectric is 1.0 mm.

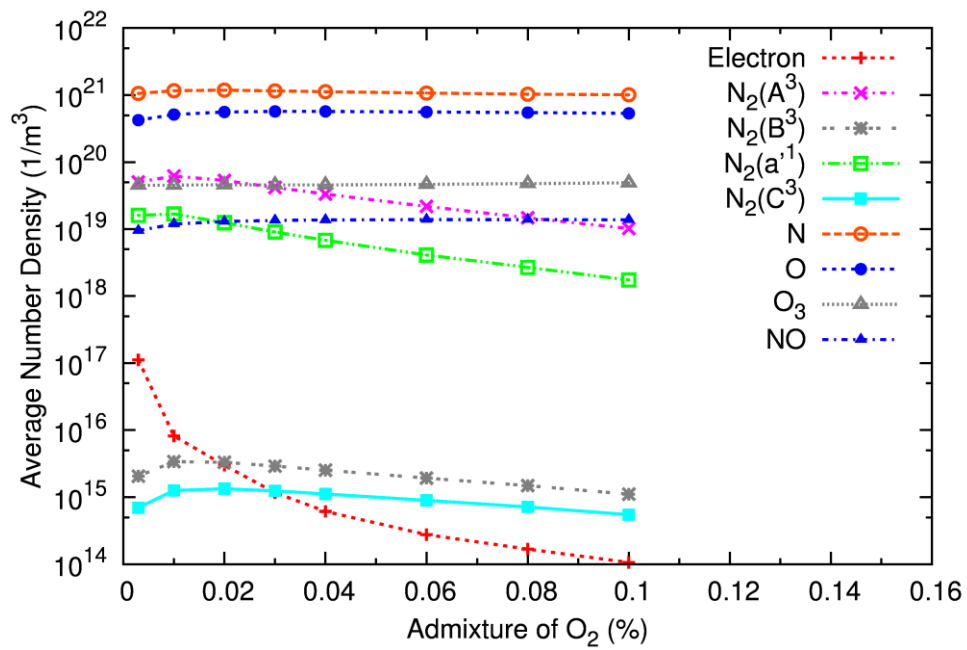


Figure 4. 5: Cycle-space averaged number densities of various admixtures of oxygen (from 0.003% to 0.1%) in nitrogen DBD, and a fixed gap distance of 1.0 mm. The quartz dielectric thickness is 1.0 mm and frequency is 60 kHz for all cases.



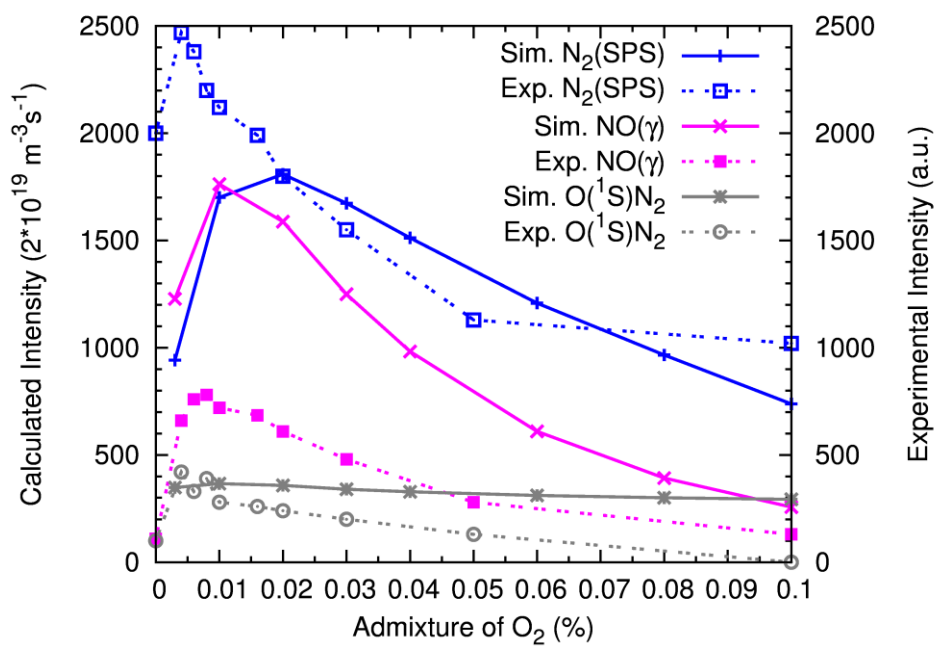


Figure 4. 6: The calculated radiations (full curves) and experimental optical emission spectrums (dashed curves) were compared as a function of the trace oxygen. The spectral bands of SPS of N<sub>2</sub>, NOγ-system and ON<sub>2</sub>-excimer were selected.

## List of Publications

### Journal Publications

1. **K.-W. Cheng**, C.-T. Hung, K.-M. Lin, Y.-M. Chiu and J.-S. Wu\*, “Investigating the Effects of Oxygen Addition on a Nitrogen-based Atmospheric Pressure Dielectric Barrier Discharge by Fluid Modeling,” Physics of Plasma, (preparing, 2012).
2. **K.-W. Cheng**, C.-T. Hung, Y.-M. Chiu and J.-S. Wu\*, “Modelling of an Atmospheric Pressure Dielectric Barrier Discharge in Nitrogen Driven by a Realistic Distorted Sinusoidal AC Power Source,” Japan Journal of Applied Physics, (under revision, 2012).
3. **K.-W. Cheng**, C.-T. Hung, M.-H. Chiang, F.-N. Hwang, J.-S. Wu\*, “One-dimensional Simulation of Nitrogen Dielectric Barrier Discharge Driven by a Quasi-Pulsed Power Source and Its Comparison with Experiments,” Computer Physics Communications, Vol. 182, pp. 164-166, 2011.
4. C.-W. Hsu, T.-C. Cheng, W.-H. Huang, J.-S. Wu\*, C.-C. Cheng, **K.-W. Cheng** and S.-C. Huang, “Relation between the Plasma Characteristics and Physical Properties of Functional Zinc Oxide Thin Film Prepared by RF Sputtering,” Thin Solid Films, Vol.518, pp. 1953-1957, 2010.
5. P.-Y. Chen, K.-H. Hsu, **K.-W. Cheng**, C.-T. Hung, J.-S. Wu\*, T.-C. Cheng and J.-P. Yu, “Modeling of the integrated magnetic focusing and gated field-emission device with single carbon nanotube,” Journal of Vacuum Science and Technology-B, Vol. 25, Issue , pp. 74-81, 2007. This article was selected for the Virtual Journal of Nanoscale Science & Technology - January 15, 2007, Volume 15, Issue 2. <http://www.vjnano.org>
6. P.-Y. Chen, Y.-L. Shao, **K.-W. Cheng**, K.-H. Hsu and J.-S. Wu\*, “Three-dimensional Simulation Studies on Electrostatic Predictions for Carbon Nanotube Field Effect Transistors,” Computer Physics Communications, Vol. 177, pp. 683-688, 2007.

## International Conference Papers

1. **K.-W. Cheng**, C.-T. Hung, Y.-M. Chiu, J.-S. Wu\*, “Numerical Investigation of Effects of Oxygen Addition on a Nitrogen-based Dielectric Barrier Discharge”, 7<sup>th</sup> International Conference on Flow Dynamics, Sendai, Japan, November 1-3, 2010. (Oral presentation)
2. **K.-W. Cheng**, C.-T. Hung, M.-H. Chiang, F.-N. Hwang, J.-S. Wu\*, “One-dimensional Simulation of Nitrogen Dielectric Barrier Discharge Driven by a Quasi-Pulsed Power Source and Its Comparison with Experiments,” Computer Physics Communications, Vol. 182, pp. 164-166, 2011. (Oral presentation)
3. C.-W. Hsu, T.-C. Cheng, W.-H. Huang, J.-S. Wu\*, C.-C. Cheng, **K.-W. Cheng** and S.-C. Huang, “Relation between the Plasma Characteristics and Physical Properties of Functional Zinc Oxide Thin Film Prepared by RF Sputtering,” Thin Solid Films, Vol.518, pp. 1953-1957, 2010.

